Cell Reports

Article

Hepatitis C virus drugs that inhibit SARS-CoV-2 papain-like protease synergize with remdesivir to suppress viral replication in cell culture

Graphical abstract

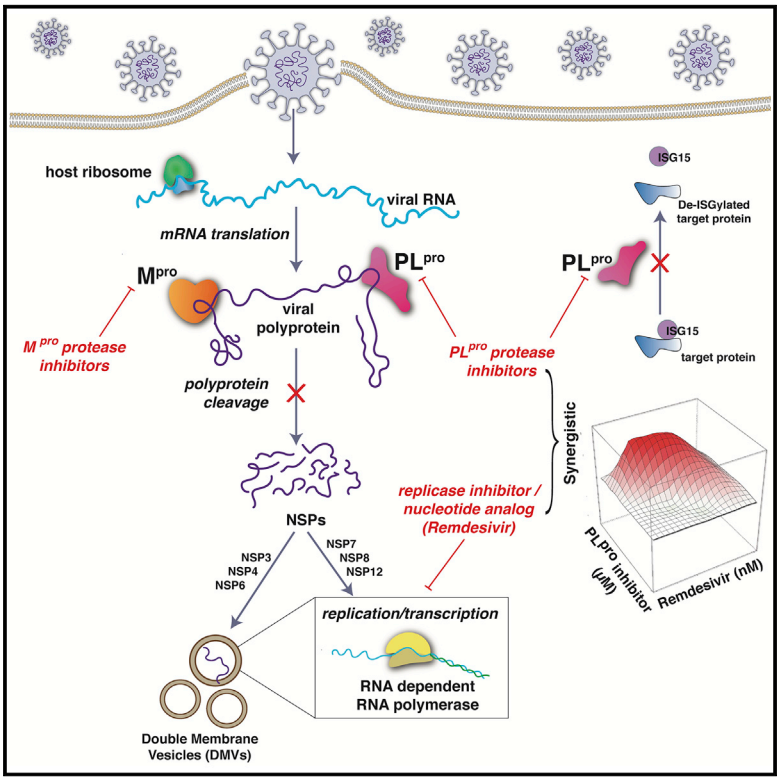

Highlights

- Several HCV protease-inhibitor drugs inhibit SARS-CoV-2 M^{pro} and/or PL^{pro}
- These HCV drugs also inhibit SARS-CoV-2 replication in Vero and/or human cells
- HCV drugs that inhibit PL^{pro} synergize with remdesivir to inhibit SARS-CoV-2
- HCV drugs that selectively inhibit M^{pro} are not synergistic with remdesivir

Authors

Khushboo Bafna, Kris White, Balasubramanian Harish, ..., Adolfo García-Sastre, Robert M. Krug, Gaetano T. Montelione

Correspondence

adolfo.garcia-sastre@mssm.edu (A.G.-S.),
rkrug@austin.utexas.edu (R.M.K.),
monteg3@rpi.edu (G.T.M.)

In brief

Bafna et al. report that several available hepatitis C virus drugs inhibit the SARS-CoV-2 M^{pro} and/or PL^{pro} proteases and SARS-CoV-2 replication in cell culture. The four HCV drugs that inhibit PL^{pro} enzyme activity also synergize with remdesivir to inhibit virus replication, increasing the antiviral activity of remdesivir and HCV drugs.

Bafna et al., 2021, Cell Reports *35*, 109133
May 18, 2021
https://doi.org/10.1016/j.celrep.2021.109133

CellPress

Cell Reports

CellPress
OPEN ACCESS

Article

Hepatitis C virus drugs that inhibit SARS-CoV-2 papain-like protease synergize with remdesivir to suppress viral replication in cell culture

Khushboo Bafna,[1,7] Kris White,[2,7] Balasubramanian Harish,[3] Romel Rosales,[2] Theresa A. Ramelot,[1] Thomas B. Acton,[1] Elena Moreno,[2] Thomas Kehrer,[2] Lisa Miorin,[2] Catherine A. Royer,[3] Adolfo García-Sastre,[2,4,5,*] Robert M. Krug,[6,*] and Gaetano T. Montelione[1,8,*]

[1]Department of Chemistry and Chemical Biology, and Center for Biotechnology and Interdisciplinary Sciences, Rensselaer Polytechnic Institute, Troy, NY 12180, USA
[2]Department of Microbiology, and Global Health and Emerging Pathogens Institute, Icahn School of Medicine at Mount Sinai, New York, NY 10029, USA
[3]Department of Biology, and Center for Biotechnology and Interdisciplinary Sciences, Rensselaer Polytechnic Institute, Troy, NY 12180, USA
[4]Department of Medicine, Division of Infectious Diseases, Icahn School of Medicine at Mount Sinai, New York, NY 10029, USA
[5]The Tisch Cancer Institute, Icahn School of Medicine at Mount Sinai, New York, NY 10029, USA
[6]Department of Molecular Biosciences, John Ring LaMontagne Center for Infectious Disease, Institute for Cellular and Molecular Biology, University of Texas at Austin, Austin, TX 78712, USA
[7]These authors contributed equally
[8]Lead contact
*Correspondence: adolfo.garcia-sastre@mssm.edu (A.G.-S.), rkrug@austin.utexas.edu (R.M.K.), monteg3@rpi.edu (G.T.M.)
https://doi.org/10.1016/j.celrep.2021.109133

SUMMARY

Effective control of COVID-19 requires antivirals directed against SARS-CoV-2. We assessed 10 hepatitis C virus (HCV) protease-inhibitor drugs as potential SARS-CoV-2 antivirals. There is a striking structural similarity of the substrate binding clefts of SARS-CoV-2 main protease (M^{pro}) and HCV NS3/4A protease. Virtual docking experiments show that these HCV drugs can potentially bind into the M^{pro} substrate-binding cleft. We show that seven HCV drugs inhibit both SARS-CoV-2 M^{pro} protease activity and SARS-CoV-2 virus replication in Vero and/or human cells. However, their M^{pro} inhibiting activities did not correlate with their antiviral activities. This conundrum is resolved by demonstrating that four HCV protease inhibitor drugs, simeprevir, vaniprevir, paritaprevir, and grazoprevir inhibit the SARS CoV-2 papain-like protease (PL^{pro}). HCV drugs that inhibit PL^{pro} synergize with the viral polymerase inhibitor remdesivir to inhibit virus replication, increasing remdesivir's antiviral activity as much as 10-fold, while those that only inhibit M^{pro} do not synergize with remdesivir.

INTRODUCTION

Effective control of the SARS-CoV-2 coronavirus that causes COVID-19 requires antivirals. Considering the urgency to identify effective antiviral drugs, and the usually lengthy process involved in approving candidate drugs for human use, our goal is to identify existing drugs already approved for use in humans that can be repurposed as safe and effective therapeutics for treating COVID-19 infections, and which may also be useful as lead molecules for novel drug development.

SARS-CoV-2 is an enveloped RNA virus, which causes COVID-19 (Wu et al., 2020). Its genome comprises a single, large positive-sense single-stranded RNA, which is directly translated by host cell ribosomes. The SARS-CoV-2 genome encodes 4 structural proteins, 16 non-structural proteins (NSPs), which carry out crucial intracellular functions, and 9 accessory proteins (Gordon et al., 2020; Wu et al., 2020). Many of these proteins, and their host binding partners, are potential targets for development of antivirals for SARS-CoV-2. For example, the repurposed drug remdesivir, which inhibits the viral RNA-dependent RNA polymerase, is the current FDA-approved antiviral standard of care for COVID-19 (Eastman et al., 2020; Pan et al., 2020).

Translation of the viral genomic RNA results in the biosynthesis of two polyproteins that are processed into the 16 separate NSPs by two virus-encoded cysteine proteases, the papain-like protease (PL^{pro}) and a 3C-like protease ($3CL^{pro}$). The latter is also referred to as the main protease (M^{pro}). M^{pro} and PL^{pro} are essential for the virus life cycle and hence are attractive targets for antiviral development. These two viral proteases are required for the production of functional viral RNA polymerases. M^{pro} cleavages are predicted to generate several NSPs, including the three subunits nsp7, nsp8, and nsp12 that constitute the viral RNA polymerase complex (Peng et al., 2020), as well as integral membrane proteins nsp4 and nsp6. PL^{pro} cleavages generate other NSPs, including nsp3 (Harcourt et al., 2004). The nsp3-nsp4-nsp6 complex is a key component of the replication organelles, also known as double-membrane vesicles (DMVs), that are required for the function of the viral polymerase in infected cells (Angelini et al.,

2013; Gosert et al., 2002; Oudshoorn et al., 2017; Snijder et al., 2020; Wolff et al., 2020a, 2020b). Considering that both M^{pro} and PL^{pro} generate either the RNA polymerase itself or the replication organelles required for polymerase function, we reasoned that inhibitors of one or both of these proteases might be synergistic with inhibitors of the viral polymerase, such as remdesivir.

We observed that the substrate binding cleft and active site of the SARS-CoV-2 M^{pro} have remarkable structural similarity with the active site of the hepatitis C virus (HCV) NS3/4A protease, suggesting that drugs that inhibit the HCV protease might also inhibit SARS-CoV-2 M^{pro} (Bafna et al., 2020). Consistent with this hypothesis, subsequent studies have reported that three of these HCV drugs, boceprevir, narlaprevir, and telaprevir, inhibit M^{pro} proteolytic activity and bind into its active site (Anson et al., 2020; Fu et al., 2020; Kneller et al., 2020a; Ma et al., 2020). Boceprevir has also been reported to inhibit SARS-CoV-2 replication in Vero cells (Anson et al., 2020; Fu et al., 2020; Ma et al., 2020). Other HCV protease inhibitors have also been reported to inhibit M^{pro} proteolytic activity (Anson et al., 2020; Fu et al., 2020; Lo et al., 2021; Ma et al., 2020) and/or viral replication (Lo et al., 2021) to various extents, while other studies report that some of these same HCV protease inhibitors did not significantly inhibit M^{pro} (Fu et al., 2020).

In this study, we assess the ability of 10 available HCV protease inhibitors to suppress SARS-CoV-2 replication. Virtual docking experiments predict that all 10 of these HCV drugs can bind snuggly into the M^{pro} binding cleft with docking scores comparable to a known M^{pro} inhibitor, suggesting that any of these 10 HCV drugs are potential inhibitors of M^{pro}. Seven of these HCV drugs inhibit both SARS-CoV-2 M^{pro} protease activity, and SARS-CoV-2 virus replication in Vero and/or human 293T cells expressing the SARS-CoV-2 ACE2 receptor. Surprisingly, we found that four HCV drugs also inhibit PL^{pro} protease activity (including one that did not inhibit M^{pro}). Consequently, HCV drugs that inhibit M^{pro} and/or PL^{pro} can suppress SARS-CoV-2 virus replication, *viz*, boceprevir (BOC), narlaprevir (NAR), vaniprevir (VAN), telaprevir (TEL), paritaprevir (PAR), simeprevir (SIM), grazoprevir (GRZ), and asunaprevir (ASU).

Further, we demonstrate that the four HCV drugs that inhibit the proteolytic activity of PL^{pro}, SIM, GRZ, PAR, and VAN, also act synergistically with remdesivir to inhibit SARS-CoV-2 virus replication, thereby increasing remdesivir antiviral activity as much as 10-fold. In addition, the PL^{pro} -specific inhibitor, GRL0617, also synergizes with remdesivir. In contrast, the HCV drugs BOC and NAR, which inhibit M^{pro} but not PL^{pro}, as well as the M^{pro}-specific inhibitor GC-376, act additively rather than synergistically with remdesivir to inhibit virus replication. Our results suggest that the combination of a HCV protease inhibitor with a RNA polymerase inhibitor could potentially function as an antiviral against SARS-CoV-2. More generally, our results strongly motivate further studies of the potential use of PL^{pro} protease inhibitors in combination with RNA polymerase inhibitors as antivirals against SARS-CoV-2.

RESULTS

Similarity of the substrate-binding clefts and active sites of SARS-CoV-2 M^{pro} and HCV protease NS3/4A

The SARS-CoV-2 main protease (M^{pro}) is a 67.6 kDa homodimeric cysteine protease with three domains (Jin et al., 2020; Zhang et al., 2020b). Domains I and II adopt a double β-barrel fold, with the substrate binding site located in a shallow cleft between two antiparallel β-barrels of domains I and II. The fold architecture of domains I and II are similar to picornavirus cysteine proteases and chymotrypsin serine proteases (Anand et al., 2002; Gorbalenya et al., 1989). A three-dimensional structural similarity search of the Protein Data Bank using the *DALI* program (Holm and Sander, 1993, 1999), with domains I and II (excluding domain III) of the SARS-CoV-2 M^{pro} as the query, identified several proteases, including the HCV NS3/4A serine protease, as structurally similar. These HCV and SARS-CoV-2 enzymes have a structural similarity *Z* score (Holm and Sander, 1993, 1999) of +8.4 and overall backbone root-mean-square deviation for structurally similar regions of ~3.1 Å. Superimposition of the analogous backbone structures of these two proteases results in superimposition of their substrate binding clefts and their active-site catalytic residues, His41/Cys145 of the SARS-CoV-2 M^{pro} cysteine protease and His57/Ser139 of the HCV NS3/4A serine protease (Figure 1A). Because of these structural similarities, we proposed that some HCV protease inhibitors might bind well into the substrate-binding cleft of the SARS-CoV-2 M^{pro} and inhibit virus replication (Bafna et al., 2020).

HCV protease inhibitors are predicted to bind into the substrate binding cleft of M^{pro}

Based on these structural similarities, we carried out docking simulations of 10 HCV NS3/4A protease inhibitor drugs (Özen et al., 2019), using *AutoDock* (Forli et al., 2016; Morris et al., 2009). These 10 drugs have been approved for at least phase 1 clinical trials, and some are FDA-approved prescription drugs used to treat HCV-infected patients (Table 1). To test the validity of our docking protocol, we first carried out docking of a previously described inhibitor of the SARS-CoV-2 M^{pro}, compound 13b (Figure S1A), that also inhibits virus replication (Zhang et al., 2020a, 2020b). Details of these control docking studies are provided in the STAR Methods and Figures S1B–S1D. The resulting docking scores are summarized in Figure 1B and Table S1. These results demonstrate that all 10 of these HCV protease inhibitors have the potential to bind snuggly into the binding cleft of M^{pro}, with extensive hydrogen-bonded and hydrophobic contacts, and predicted *AutoDock* energies of −8.37 to −11.01 kcal/mol, comparable to those obtained for M^{pro} inhibitor 13b (~ −9.0 kcal/mol).

The 1.44-Å X-ray crystal structure of the complex of BOC bound to the SARS-CoV-2 M^{pro} was recently released in the Protein Data Bank [PDB: 6WNP (Anson et al., 2020; Anson and Mesecar, 2020)]. The BOC pose observed in this X-ray crystal structure is almost identical to the lowest energy pose (−9.13 kcal/mol) predicted by *AutoDock* (Figure 1C). In addition, both the docked and crystal structure binding poses for BOC near the active site of M^{pro} are very similar to its binding pose in the substrate binding cleft of HCV protease (Figure 1D), with an essentially identical hydrogen-bonding network between BOC and corresponding residues in each protease (shown in Figures S1E and S1F). Recently, Kneller et al. (2020a) also reported an X-ray crystal structure of the SARS-CoV2 M^{pro}-BOC complex, as well as the structures of M^{pro} complexed with HCV inhibitors NAR and TEL. The predicted binding modes of

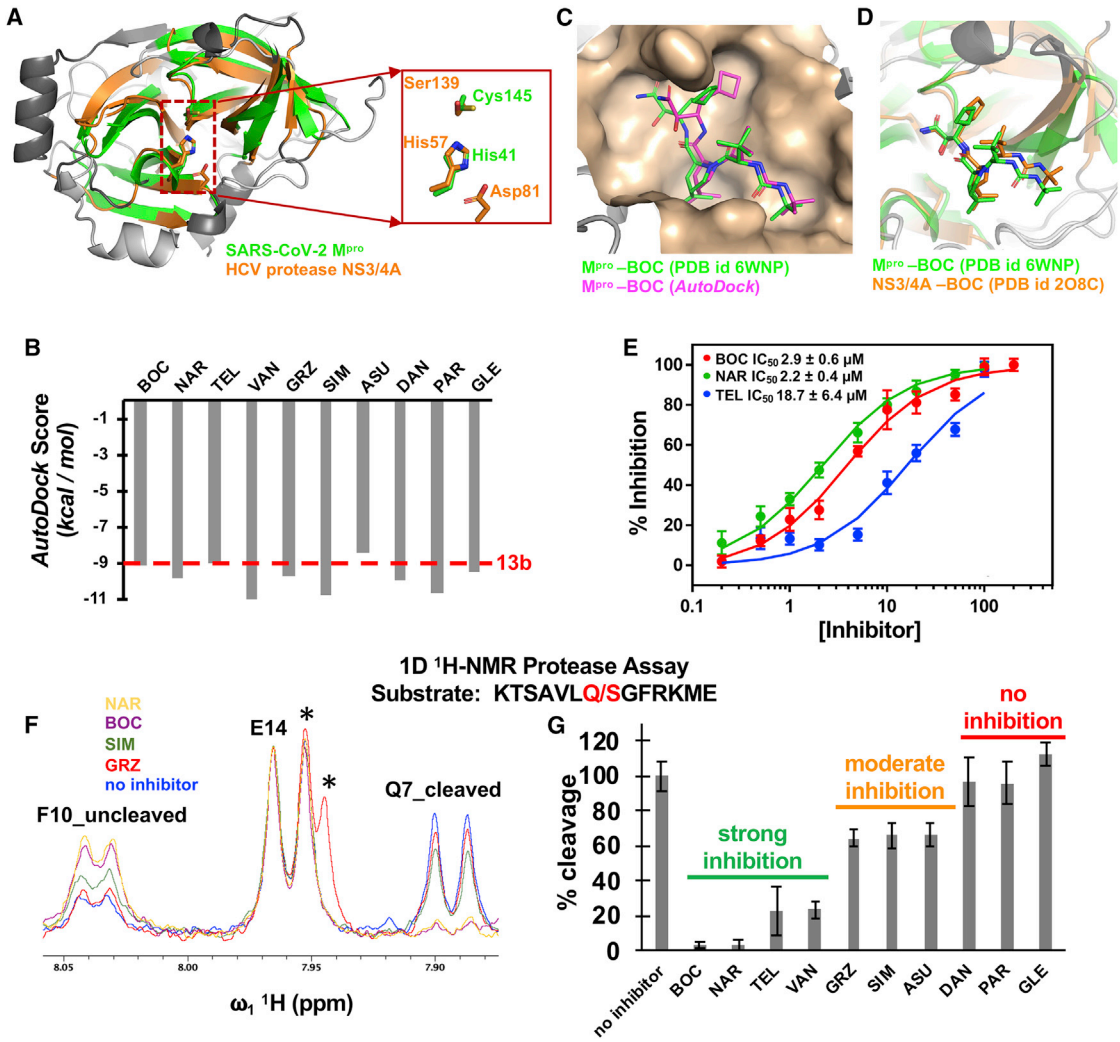

Figure 1. SARS-CoV-2 M^{pro} binds HCV NS3/4A protease inhibitors

(A) The active site cleft of the SARS-CoV-2 M^{pro} (green, PDB: 6Y2G) has remarkable structural similarity with the active site cleft of HCV protease NS3/4A (orange, PDB: 2P59). Both have a double β-barrel fold architecture, with a substrate binding site located in a shallow cleft between two the antiparallel β-barrels. The regions identified by DALI as structurally analogous are shown in color (green and orange), and the regions that are not structurally analogous are shown in gray. This superimposition of backbone atoms results in superimposition of the catalytic residues Cys145 and His41 of the SARS-CoV-2 M^{pro} with Ser139 and His57 of HCV protease. Asp81 of the HCV protease catalytic triad is also shown.

(B) Best *AutoDock* docking scores for 10 HCV protease inhibitors in the substrate binding cleft of SARS-CoV-2 M^{pro}. Each docking trajectory was run one-hundred times. The best docking score for M^{pro} inhibitor 13b is shown as a horizontal red dashed line.

(C) Comparison of the BOC binding pose in best-scoring *AutoDock* complex (magenta) with the X-ray crystal structure of the BOC-M^{pro} complex (Anson and Mesecar, 2020) (green, PDB: 6WNP).

(D) Comparison of BOC binding poses in X-ray crystal structures of complexes with HCV NS3/4A protease (orange, PDB: 2OC8; (Prongay et al., 2007)) and SARS-CoV-2 M^{pro} protease (green, PDB: 6WNP).

(E) Dose-response curves based on FRET assay for inhibition of M^{pro}, by NAR, BOC, and TEL.

(F) 1D ^{1}H-NMR assay for hydrolysis of the indicated peptide substrate. The amide proton doublets of Phe-10 prior to cleavage (F10_uncleaved) or of Gln-7 after cleavage (Q7_cleaved) provide well-resolved resonances for monitoring the proteolysis reaction. The amide proton doublet of Glu-14 (E14) is not perturbed by cleavage and provides an internal intensity calibration control. GRZ has resonances (labeled by *) that overlap with the upfield component of the E14 doublet.

(G) Percentage of cleavage of the indicated peptide substrate by M^{pro} after 30 min at 25°C. FRET data points are mean ± SD, n = 3; NMR resonance ratio uncertainties were based on signal-to-noise measurements.

See also Tables S1–S3 and Figures S1–S4 and S7.

BOC and NAR are also an excellent match to these subsequently determined experimental structures (Figures S1G and S1H), while for TEL poses similar to the crystal structure are included among the best-scoring *AutoDock* poses (Figures S1I and S1J). BOC, NAR, and TEL are alpha-ketoamides which form covalent bonds with the active site residue Cys145 of M^{pro}.

Table 1. HCV protease inhibitors

Inhibitor (trade name)	Identifier of protease inhibitor	Trade name; manufacturer	Drug status
Vaniprevir	VAN	MK-7009; Merck	investigational drug
Simeprevir	SIM	Olysio/Medivir; Janssen	prescription drug
Paritaprevir	PAR	Veruprevir/ABT-450; Abbott Laboratories	prescription drug
Danoprevir	DAN	Ganovo; Array/Pfizer, Roche/Ascletis	investigational drug
Narlaprevir	NAR	Arlansa; Merck/R-Pharm	prescription drug
Grazoprevir	GRZ	Zepatier; Merck	prescription drug
Glecaprevir	GLE	Mavyret[a] Maviret[a]; AbbVie/Enanta	prescription drug
Boceprevir	BOC	Victrelis; Merck	prescription drug
Telaprevir	TEL	Incivek/Incivo; Vertex/J&J	prescription drug
Asunaprevir	ASU	Sunvepra; Bristol-Myers Squibb	investigational drug

[a]Mavyret (or Maviret) is a multidrug formulation including glecaprevir and pibrentasvir.

Although this docking protocol does not include energetics or restraints for covalent bond formation, in the low-energy poses of both BOC and NAR bound to M^{pro}, the alpha-keto amide carbon is positioned within 3.8 Å of the active site thiol sulfur atom. These blind tests support the predictive value of docking results for the other HCV protease inhibitors. From these virtual docking studies and comparison with subsequently determined X-ray crystal structures, we conclude that all 10 of these HCV protease inhibitors have the potential to bind into the substrate-binding cleft of M^{pro}, and to inhibit binding of its substrates.

Seven HCV drugs inhibit M^{pro} protease activity

Inhibition activity of HCV drugs against M^{pro} was initially assessed using a protease assay based on Föster resonance energy transfer (FRET) using the peptide substrate Dabsyl-KTSAVLQ/SGFRKME-(Edans), containing a canonical M^{pro} protease recognition site. Under the conditions of these FRET assays, there is little or no inner filter effect for most of the drug-peptide substrate assays (Table S3), and the half-life for the proteolytic reaction is about 30 min (Figures S2A and S2B). HCV protease inhibitors NAR, BOC, and TEL have significant enzyme inhibition activity, with IC_{50} values of 2.2 ± 0.4 μM, 2.9 ± 0.6 μM, and 18.7 ± 6.4 μM, respectively (Figure 1E). In contrast, little or no inhibition activity was detected in this FRET assay with the other seven HCV protease inhibitors (Figures S3A and S3B).

We also developed a 1D ^{1}H-NMR assay, using the peptide substrate KTSAVLQ/SGFRKME that lacks the Dabsyl and Edans N-terminal and C-terminal tags (Figure S4). In this 1D ^{1}H-NMR assay, NAR, BOC, and TEL have substantial enzyme inhibition activity, as was the case in the FRET assay. In addition, in the NMR assay substantial inhibitory activity was also observed for VAN, and moderate inhibitory activity was observed for GRZ, SIM, and ASU (Figures 1F and 1G). This significant inhibition activity of VAN, and moderate inhibition activities of GRZ, SIM, and ASU, was not detected in the FRET assay. DAN, PAR, and GLE had little or no detectable M^{pro} inhibitory activity. From these studies, we conclude that seven HCV drugs (*viz* BOC, NAR, TEL, VAN, GRZ, SIM, and ASU) inhibit SARS-CoV-2 M^{pro} strongly or moderately under the conditions tested.

Eight HCV drugs inhibit SARS-CoV-2 replication in Vero and/or human 293T cells

The motivation for the docking and biophysical studies described above was to identify HCV drugs with the potential to inhibit SARS-CoV-2 virus replication. For antiviral assays, Vero E6 cells or human 293T cells expressing the ACE2 receptor, were grown in 96-well plates and were incubated with various levels of a HCV protease inhibitor for 2 h. Cells were then infected with SARS-CoV-2 virus at the indicated multiplicity of infection (MOI, plaque-forming units [PFU]/cell) and incubated for the indicated times at 37°C in the presence of the inhibitor. Virus-infected cells were identified by immunofluorescence using an antibody specific for the viral nucleoprotein. Inhibition of viral replication was quantified by determining the percentage of positive infected cells at the end of the incubation period in the presence of the compound, as compared with the number of infected cells in its absence. To determine whether a HCV drug was cytotoxic, uninfected Vero E6 or human 293T cells were incubated with the same levels of the compounds for the same length of time, and cytotoxicity was measured using an MTT assay (Roche). In all of these replication assays, remdesivir was used as a positive control.

Viral replication inhibition data in Vero E6 cells are summarized in Figure 2; Table S2. Five of the HCV protease inhibitors tested, PAR, NAR, GRZ, ASU, and BOC, inhibited SARS-CoV-2 virus replication at concentrations significantly lower than the concentrations that cause cytotoxicity. Two other HCV protease inhibitors, SIM and VAN, inhibited virus replication with low IC_{50} values, but some cytotoxicity was also observed. These seven HCV drugs have IC_{50} values for inhibiting SARS-CoV-2 replication of 4.2 to 19.6 μM. The remaining three HCV drugs tested, TEL, GLE, and DAN, did not inhibit virus replication in Vero E6 cells, even at a drug concentration of 50 μM.

Next, we also determined whether the HCV drugs exhibited similar antiviral activities in human cells, specifically human 293T cells expressing the ACE2 receptor (Figure 3; Table S2). Again, PAR, SIM, and VAN were the most effective inhibitors of virus replication, with IC_{50} values of 0.55 to 3.0 μM, and with considerably reduced cytotoxicity as compared to assays in Vero cells. BOC and NAR, which are relatively strong M^{pro} inhibitors (Figures 1E–1G), were less effective inhibitors of virus replication, with IC_{50}s of 5.4 and 15 μM. The other covalent M^{pro} inhibitor, TEL, which did not inhibit in Vero cells had a IC_{50} of 20.5 μM in human cells, while GRZ had less potent antiviral activity in human cells than in Vero cells (cf. Figures 2F, 2I, 3G, and 3H). Thus, seven HCV drugs inhibited SARS-CoV-2 replication in human 293T cells, with IC_{50} values ranging from 0.55 to 20.5 μM. GLE and DAN did not inhibit virus replication in human cells, as was also the case in Vero cells. ASU, a modest inhibitor

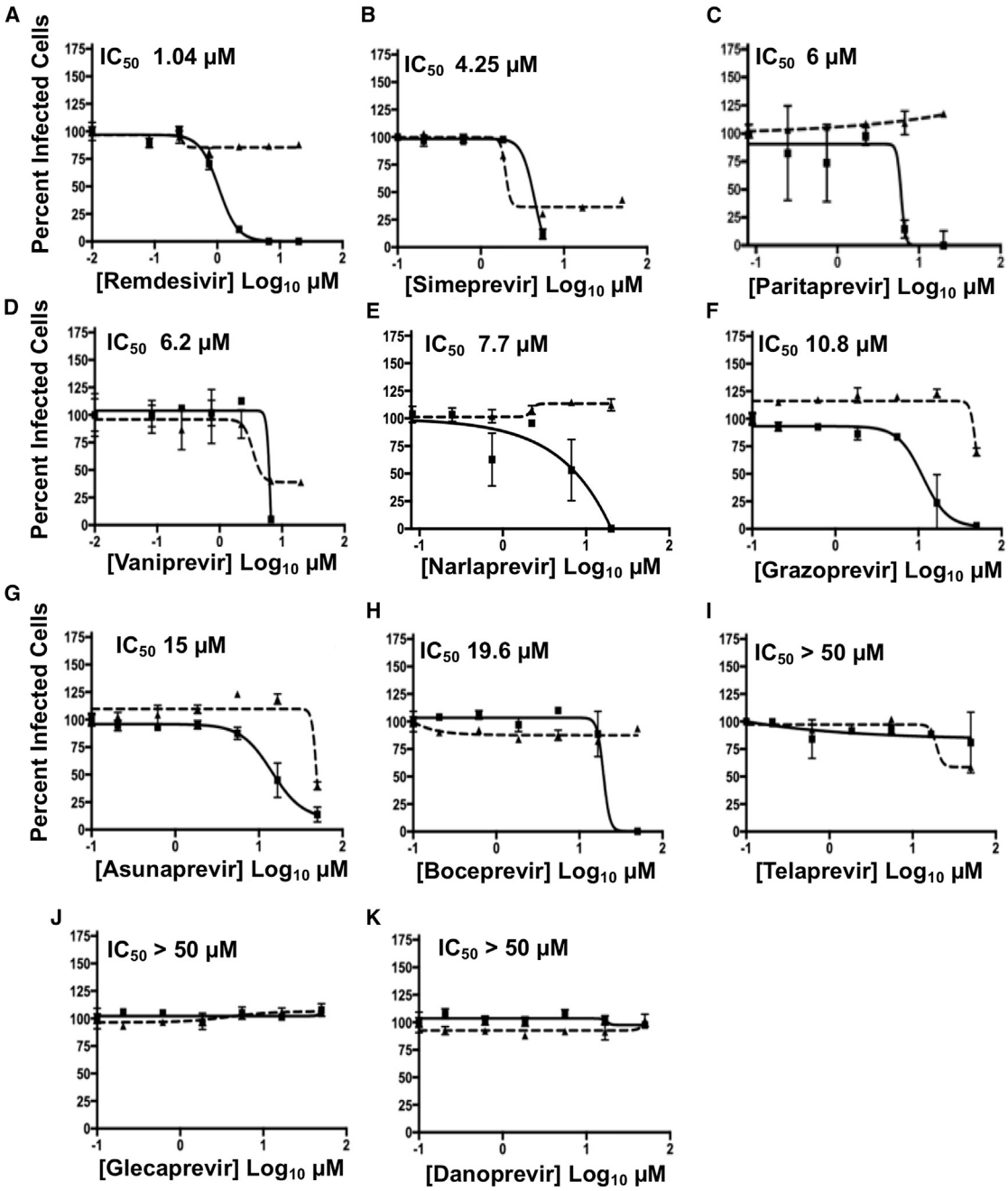

Figure 2. Antiviral activity of HCV protease inhibitors in Vero E6 cells

(A–K) Inhibition of viral replication was determined in a concentration-dependent matter in Vero E6 cells. Replication assays were performed at MOI of 0.025 PFU/cell. In all panels, viral infectivity is shown as a solid line and cell toxicity as a dashed line. Data = mean ± SD; n = 3 independent samples. The estimated IC_{50} is labeled in the top-left corner of each plot. Remdesivir is included as a standard of care control. See also Table S2.

in Vero cells, did not inhibit viral replication in human cells at concentrations lower than those exhibiting cytotoxicity.

We also determined whether the inhibition of SARS-CoV-2 replication by representative HCV protease inhibitors occurs at steps after virus entry, as would be expected for inhibitors of viral proteases that are produced after infection. Accordingly, we performed time-of-addition assays in human cells, using BOC (50 μM), GRZ (25 μM), NAR (50 μM), VAN (5 μM), and SIM (5 μM), at concentrations that do not show detectable cytotoxicity as measured by MTT assay (Table S2) or by DAPI staining in infected cells. In a single cycle (MOI of 2 PFU/cell over a total infection time of 8 h) of infection, drugs were added 2 h prior to infection, at the time of infection, or at 2 or 4 h post-infection. Virus replication was inhibited by the addition of these drugs as

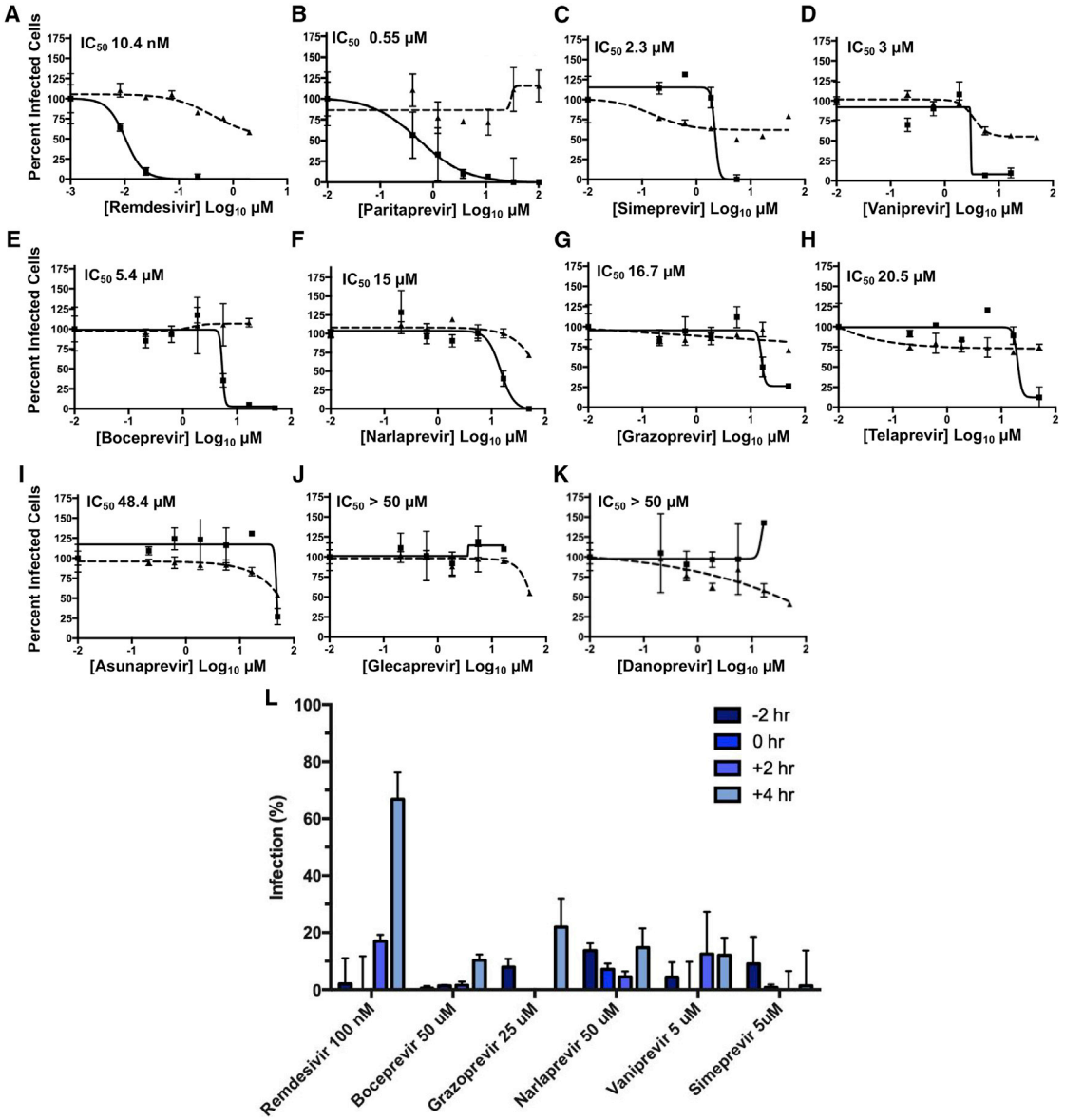

Figure 3. Antiviral activity of HCV protease inhibitors in HEK293T cells

(A–K) Inhibition of viral replication was determined in a concentration-dependent matter in human 293T cells. Replication assays were performed at MOI of 0.025 PFU/cell. In all panels, viral infectivity is shown as a solid line and cell toxicity as a dashed line. Calculated IC_{50} is indicated in the top-left corner of each plot. Remdesivir is included as a standard of care control.

(L) Time-of-addition assay in human 293T cells. Drugs, at the indicted non-cytotoxic concentrations, were added to cells at the indicated time points before (–2 h), at (0 h), or after (+2 or +4 h) viral infection, at MOI of 2 PFU/cell.

Data are mean ± SD; n = 3 independent samples.

See also Table S2.

late as 4 h post-infection (Figure L), indicating that these drugs can inhibit viral infection after the initial phase of virus entry. These results indicate that these HCV drugs inhibit virus-encoded proteases synthesized in infected cells. The results do not, however, rule out that these drugs may also inhibit other proteases or enzymes, including any involved in virus entry. In contrast, addition of the RNA polymerase inhibitor remdesivir 4 h after the initiation of infection decreased its ability to suppress virus infection, demonstrating the crucial role of viral RNA synthesis at early times of infection.

Simeprevir and grazoprevir synergize with remdesivir to increase inhibition of SARS-CoV-2 virus replication

Because M^{pro} and PL^{pro} generate either the RNA polymerase itself or the proteins that constitute the replication organelles required for polymerase function, we predicted that HCV drugs

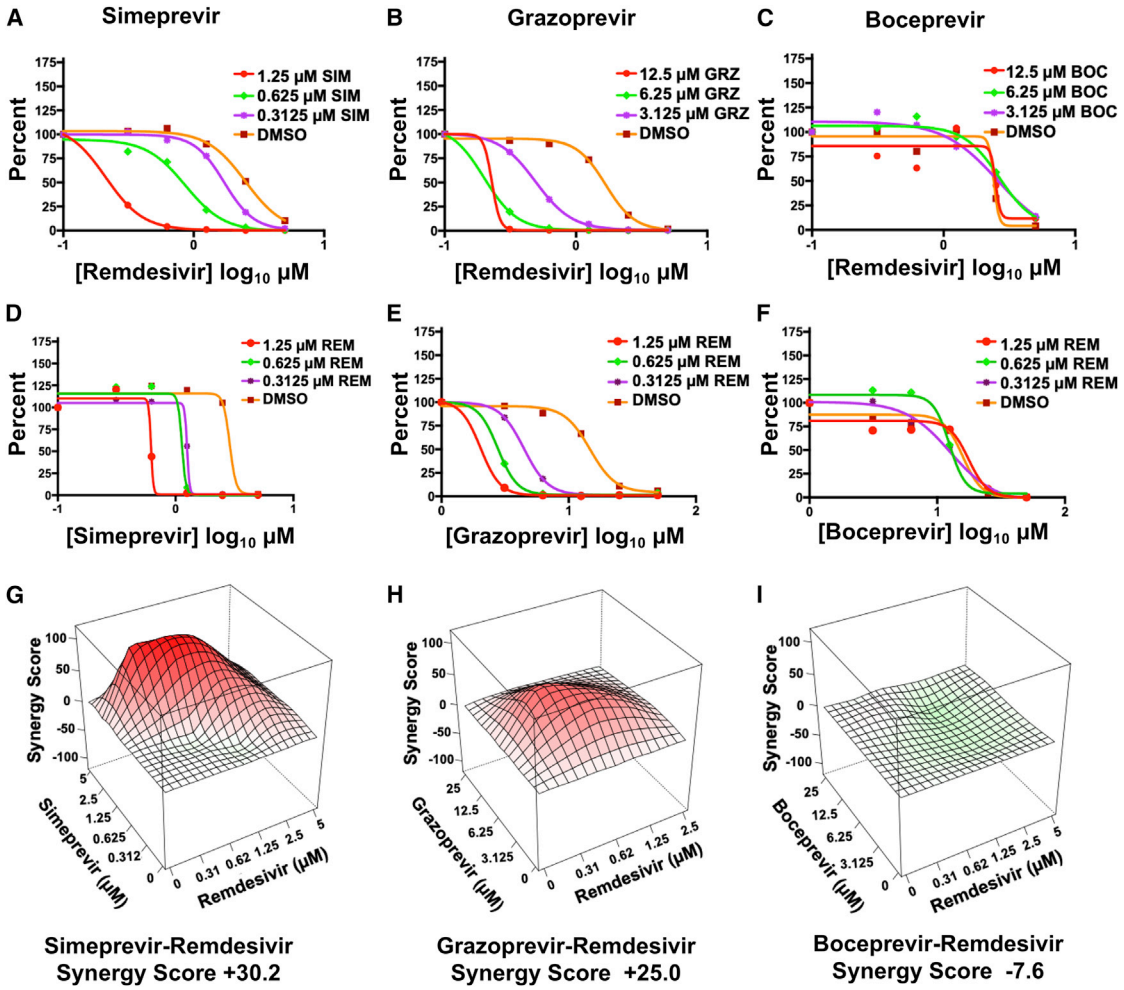

Figure 4. Simeprevir and grazoprevir are synergistic with remdesivir in Vero E6 cells

(A–C) SARS-CoV-2 inhibition by remdesivir in the presence of increasing concentrations of SIM, GRZ, or BOC.

(D–F) SARS-CoV-2 inhibition by SIM, GRZ, or BOC in the presence of increasing concentrations of remdesivir.

(G–I) Synergy landscapes and combination scores generated by the ZIP method using the program SynergyFinder (Ianevski et al., 2020).

See also Table S2 and Figure S5.

that inhibit one or both of these viral proteases might be synergistic with inhibitors of the viral polymerase like remdesivir. To test this hypothesis, we carried out antiviral combination assays of SIM, GRZ, and BOC, respectively, with remdesivir in Vero cells. To assess synergy, two analyses are required. In one analysis the IC_{90} of the remdesivir was measured in the presence of increasing concentrations of each of these three HCV drugs (Figures 4A–4C). These results demonstrate that SIM and GRZ increase the antiviral activity of remdesivir. For example, in the presence of 1.25 μM SIM, approximately 10-fold less remdesivir is required for the same antiviral effect achieved in the absence of SIM (Figure 4A). A similar 10-fold enhancement in antiviral activity of remdesivir is observed in the presence of GRZ, though at higher (6.25 μM) GRZ concentrations (Figure 4B). Surprisingly, although BOC is a much better inhibitor of M^{pro} than either SIM or GRZ, BOC did not significantly affect the antiviral activity of remdesivir (Figure 4C). In the second analysis, the IC_{90} concentration of each HCV drug was determined in the presence of increasing concentrations of remdesivir (Figures 4D–4F). Remdesivir increased the antiviral activity of SIM and GRZ. For example, addition of 1.25 μM remdesivir substantially reduces the concentration of SIM or GRZ needed to achieve IC_{90} conditions (Figures 4D and 4E). In contrast, remdesivir did not significantly affect the antiviral activity of BOC (Figure 4F).

These antiviral assays indicate that SIM and GRZ, but not BOC, act synergistically with remdesivir to inhibit virus replication. As confirmation, we subjected these results to analysis by the zero interaction potency (ZIP) model for synergy (Ianevski et al., 2020). In the landscapes generated by this model (Figures 4G–4I), red denotes a synergistic interaction, and green denotes an additive interaction. In this model a synergistic interaction between drugs has a score greater than +10, an additive interaction has a score between −10 to +10, and an antagonistic interaction has a score of less than −10. The landscapes for the interaction

of remdesivir with both SIM and GRZ are red, with synergy scores of +30.2 and +25.0, respectively, denoting moderate synergism. In contrast, the landscape for the interaction of remdesivir with BOC does not indicate synergy (Figure 4I); the synergy score, −7.6, indicates an additive interaction. We also carried out combination antiviral assays in human 293T cells. The interaction between remdesivir and GRZ in inhibiting virus replication in the human cells was also synergistic, with a red landscape and a synergy score of +20.3 (Figure S5). Consequently, at least two HCV drugs, SIM and GRZ, act synergistically with remdesivir to inhibit SARS-CoV-2 virus replication in Vero and/or human 293T cells.

Four HCV protease inhibitors that are synergistic with remdesivir inhibit PL^{pro}

The preceding results demonstrate that several HCV inhibitors inhibit viral replication, and that for some of these drugs inhibition is synergistic with the viral replication inhibition activity of remdesivir. Most of these drugs also inhibit SARS-CoV-2 M^{pro}. However, M^{pro} and SARS-CoV-2 inhibition by these drugs were not consistently correlated. For example, PAR does not inhibit M^{pro} in either the FRET or NMR assays but is an effective inhibitor of SARS-CoV-2 in both Vero (IC_{50} = 6 μM) and 293T (IC_{50} = 0.55 μM) assays. In addition, the HCV protease inhibitors SIM and GRZ, which are only moderate inhibitors of M^{pro}, synergize with remdesivir, while BOC, which is an excellent inhibitor of M^{pro}, acts additively rather than synergistically with remdesivir to inhibit virus replication. Although the lack of strong correlation between protease inhibition activity and viral inhibition activity could result from various effects, including the efficiency of transport of drugs into the cell and/or metabolism of the drugs in the cell-based assays, these results suggested that there might be a second viral target for some of these HCV drugs, for which inhibition may provide the basis for the observed synergy.

Aside from both being Cys proteases, the active site of PL^{pro} does not share structural similarity with the HCV NS3/4A or M^{pro} proteases. However, it has recently been reported that SIM, GRZ, and ASU inhibit PL^{pro} (Anson et al., 2020). Accordingly, we carried out virtual docking studies of these same 10 HCV drugs into the substrate-binding cleft of PL^{pro}, using protocols similar to those developed in virtual docking studies with M^{pro}. The known PL^{pro} inhibitor GRL0617 (Fu and Huang, 2020) was used to assess the docking protocol, providing a reference *AutoDock* score of −7.54 kcal/mol. The scores of docking poses for HCV drugs, summarized in Figure 5A and Table S1, range from –5.56 kcal/mol for BOC and NAR, to much more favorable values of < –8 kcal/mol for others, including VAN, GRZ, SIM, and PAR. These proof-of-concept docking studies suggest that, surprisingly, some HCV protease inhibitors may bind in the substrate-binding clefts of both M^{pro} and PL^{pro}.

Based on these docking predictions, we anticipated that several HCV protease inhibitors, not including BOC, NAR, or TEL, might effectively inhibit PL^{pro} protease activity. To test this hypothesis, fluorescence assays of PL^{pro} inhibition were carried out, using the substrate zRLRGG/AMC (z - carboxybenzyl; AMC - 7-Amino-4-methylcoumarin) (Anson et al., 2020) containing a natural canonical PL^{pro} protease recognition site (XLXGG). Of the HCV drugs tested, four drugs predicted to bind into the active site of PL^{pro}, VAN, SIM, PAR, and GRZ, do in fact inhibit PL^{pro} protease activity (Figure 5B; Figure S6). Hence, VAN, SIM, and GRZ inhibit both M^{pro} and PL^{pro}, while PAR inhibits PL^{pro}, but not M^{pro}. Under these assay conditions, VAN and SIM are more effective PL^{pro} inhibitors than GRZ or PAR.

These results strengthened our hypothesis that synergy between these HCV drugs and remdesivir arises primarily from their activities in inhibiting PL^{pro}, rather than from inhibiting M^{pro}. To further test this, combination assays with remdesivir were carried out also for NAR, PAR, and VAN. As predicted, PAR which moderately inhibits PL^{pro} but not M^{pro}, is synergistic with remdesivir (Figure 5C, synergy score +17.3). VAN, which inhibits both M^{pro} and PL^{pro}, is also modestly synergistic, with synergy score + 10.9, while NAR, which inhibits M^{pro} but not PL^{pro}, is additive with synergy score –3.6 (Figures 5D and 5E).

Data for HCV protease drugs on SARS-CoV-2 protease inhibition and synergy are summarized in Figure 6A and in Table S2. Two drugs, BOC and NAR, which are relatively good inhibitors of M^{pro} but do not inhibit PL^{pro}, have additive interactions with remdesivir. Three drugs, GRZ, SIM, and VAN, which inhibit both M^{pro} and PL^{pro}, are synergistic, with synergy scores of +10.9 to +30.2. Interestingly, among these three, VAN, which is a relatively strong inhibitor of both M^{pro} and PL^{pro}, has the weakest synergy. A fourth HCV drug, PAR, which inhibits PL^{pro} but not M^{pro}, also has synergy with remdesivir, with synergy score +17.3. These data demonstrate a correlation between the PL^{pro} inhibiting activities of these drugs and their ability to function synergistically with remdesivir to suppress viral replication.

In order to further test this model of synergy, we also carried out biochemical and viral replicase assays with the molecule GC-376, an M^{pro} inhibitor (Fu et al., 2020; Ma et al., 2020), and an analog of GRL0617, referred to as compound 6, an established PL^{pro} inhibitor (Fu and Huang, 2020; Osipiuk et al., 2021; Ratia et al., 2008). While GC-376 has been reported to be specific for M^{pro} relative to PL^{pro} (Sacco et al., 2020), the relative specificity of GLR0617 (or compound 6) for PL^{pro} relative to M^{pro} has not previously been reported. Using the same fluorescence assays outlined above, we validated the high specificity of GC-376 for M^{pro} inhibition compared to PL^{pro} (Figure 6B, left) and documented high specificity of compound 6 for PL^{pro} inhibition compared to M^{pro} (Figure 6B, right). As predicted, combination viral inhibition assay of GC-376 with remdesivir shows an additive interaction (Figure 6C; synergy score +5.9), while the GRL0617 analog (compound 6) has a synergistic interaction with remdesivir (Figure 6D; synergy score +18.6). We conclude that inhibitors of the SARS-CoV-2 PL^{pro} protease function synergistically with remdesivir to inhibit viral replication, whereas specific inhibitors of the M^{pro} protease act additively with remdesivir.

DISCUSSION

To provide antiviral drugs that can be rapidly deployed to combat the COVID-19 pandemic, we carried out the present study to identify currently available drugs that could potentially be repurposed as inhibitors of the SARS-CoV-2 virus that causes the COVID-19 disease. A total of eight HCV drugs were identified that inhibit virus replication in Vero and/or human 293T cells expressing the ACE2 receptor.

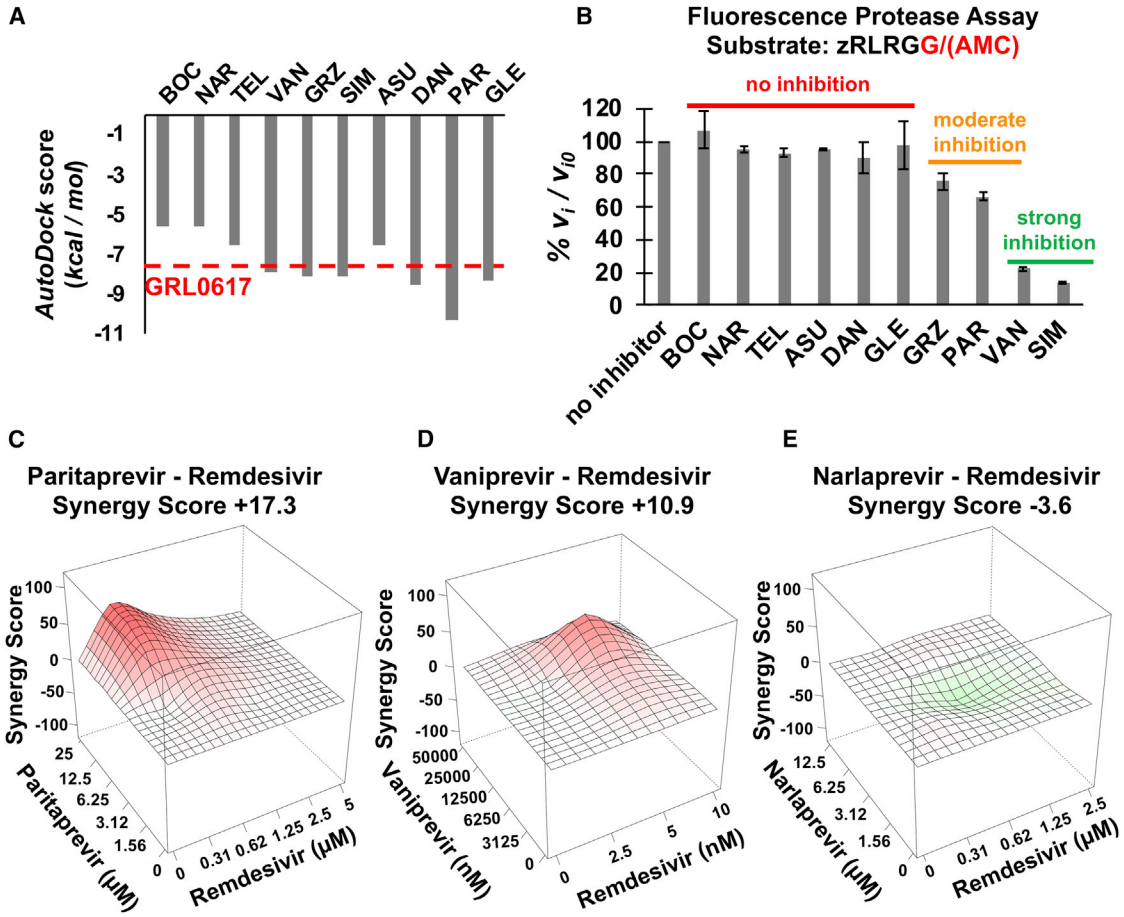

Figure 5. HCV protease inhibitors also inhibit SARS-CoV-2 PL^{pro}

(A) Best *AutoDock* docking scores for 10 HCV protease inhibitors in the substrate binding cleft of SARS-CoV-2 PL^{pro}. The docking score for PL^{pro} inhibitor GRL0617 is also shown as a horizontal red dashed line. Each docking trajectory was run one-hundred times.

(B) Initial rates of proteolysis of a peptide substrate by PL^{pro} in the presence of 20 μM inhibitor concentrations (v_i) relative to initial rate in the absence of inhibitor ($v_{i,o}$), at 25°C. GRZ inhibition of PL^{pro} was even stronger ($v_o/v_{o,i}$ = 32% ± 7%) at 100 μM drug concentration (Figure S6). Data are mean ± SD, n = 2 independent measurements.

(C and D) PL^{pro} inhibitors PAR and VAN are synergistic with remdesivir.

(E) NAR does not inhibit PL^{pro} and is also not synergistic with remdesivir.

See also Tables S2 and S3 and Figures S1 and S6.

We initiated our search based on the striking similarity of the substrate binding clefts of the SARS-CoV-2 M^{pro} and HCV NS3/4A proteases (Bafna et al., 2020). The substrate-binding clefts and active sites of M^{pro} and HCV proteases superimpose remarkably well (Figure 1A), despite having very low sequence similarity (Figure S7) and significantly different structural topologies (Bafna et al., 2020). Our virtual docking experiments showed that 10 HCV protease inhibitors can be docked snuggly into the substrate binding cleft of M^{pro} and hence have the potential to inhibit binding of the M^{pro} substrate, thereby inhibiting proteolytic cleavage of the viral polyprotein to form NSPs. For BOC and NAR, these predicted docking poses (Bafna et al., 2020) are consistent with the subsequently determined X-ray crystal structures (Anson et al., 2020; Anson and Mesecar, 2020; Kneller et al., 2020a); for TEL, some predicted binding poses are also similar to the corresponding crystal structure (Kneller et al., 2020a). Four of these HCV drugs, BOC, NAR, TEL, and VAN, are relatively strong inhibitors of SARS-CoV-2 M^{pro} protease activity (IC_{50} of 2 to ~20 μM), and three other HCV drugs, GRZ, SIM, and ASU, moderately inhibit M^{pro} activity. BOC, NAR, and TEL are α-keto amides, which can form a covalent bond with the active site Cys thiol of M^{pro} . The other four HCV drugs are non-covalent inhibitors of the M^{pro} protease and cannot form a covalent bond with the active site Cys thiol.

Other groups have also recently reported that some of these same HCV protease inhibitors can inhibit M^{pro} protease activities (Anson et al., 2020; Fu et al., 2020; Kneller et al., 2020a; Lo et al., 2021; Ma et al., 2020). While all of these studies report BOC as a moderately potent inhibitor of M^{pro}, there are inconsistent reports of the effectiveness of some of the other HCV protease inhibitors reported here as inhibitors of M^{pro} and/or PL^{pro}. These inconsistencies likely arise from details of the different assays,

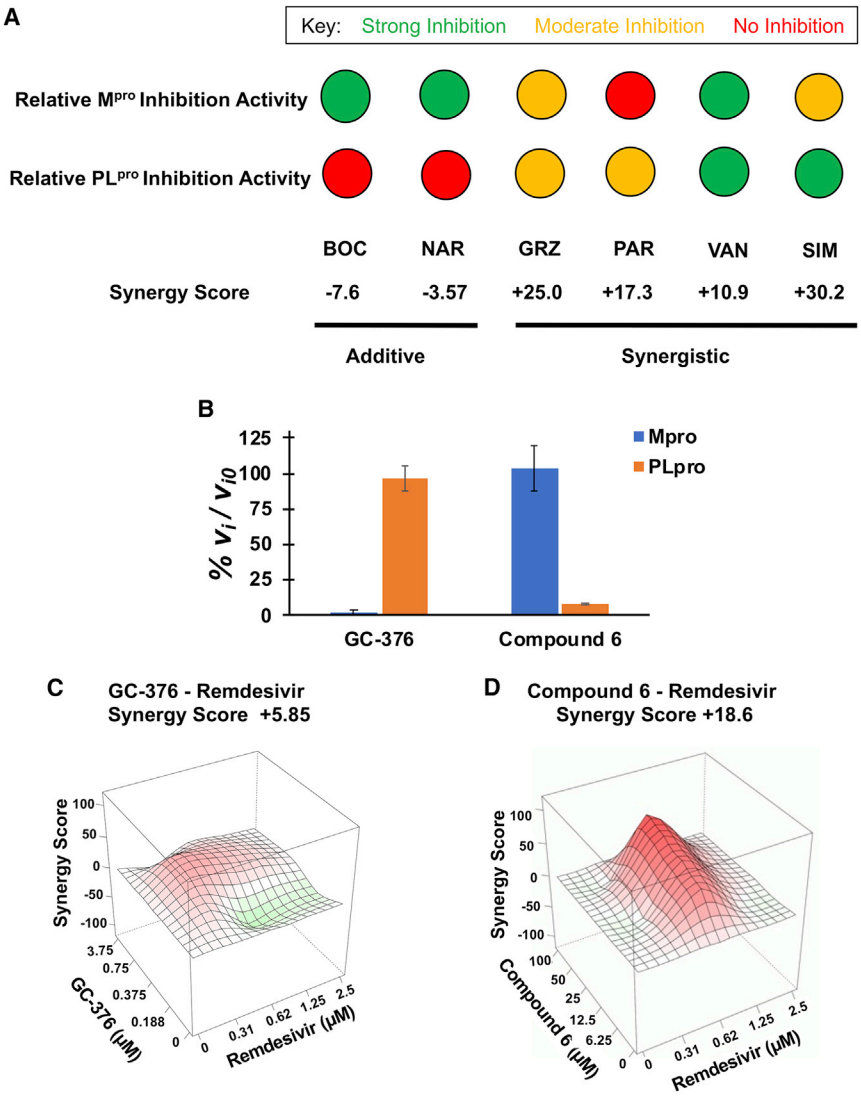

Figure 6. PL^{pro} inhibition and synergy with remdesivir activities are correlated

(A) Summary of relative inhibition of SARS-COV-2 proteases by HCV protease inhibitors and their respective synergies with remdesivir. The inset key shows the color coding for strong (green, IC_{50} < 20 μM), moderate (yellow, 20 μM < IC_{50} < 50 μM), and no (red) enzyme inhibition activity.

(B) Initial rates of proteolysis of peptide substrates by selective M^{pro} (GC-376) and PL^{pro} (compound 6) inhibitors at 20 μM concentrations (v_i), relative to initial rate in the absence of inhibitor ($v_{i,o}$), at 25°C. Data are mean ± SD, n = 2.

(C and D). Synergy landscapes and combination scores (Ianevski et al., 2020).

See also Tables S1 and S2.

including the specific protein constructs and polypeptide substrates.

The significant intrinsic fluorescence of these non-covalent inhibitor drugs complicates the M^{pro} FRET assay (see STAR Methods), particularly for VAN, SIM, and GRZ (see Figure S3A). For this reason, we also used 1D ^{1}H-NMR assay for M^{pro} inhibition, which confirmed that BOC, NAR, and TEL inhibit M^{pro}. In the NMR assay VAN also has inhibitory activity comparable to TEL, while GRZ, SIM, and ASU are moderate inhibitors of M^{pro}. The ability of the NMR assay to detect inhibitory activity that was not detected by the FRET assay is attributable to several factors, including differences in substrate and enzyme concentrations used in these assays, and differences in the substrates themselves. The ability of HCV drugs to inhibit M^{pro} also depends on other details of the assay conditions, most notably the enzyme, substrate, and drug concentrations and details of the M^{pro} construct (Grum-Tokars et al., 2008).

Although the active site of PL^{pro} does not share structural similarity with the HCV NS3/4A protease, we observe that four HCV drugs, SIM, GRZ, VAN, and PAR, inhibit PL^{pro} protease activity *in vitro*. None of these four inhibitors can form covalent bonds with the active-site Cys residue of PL^{pro}. VAN is a good inhibitor of both M^{pro} and PL^{pro}, presumably accounting for its strong inhibition of virus replication. All four of these HCV drugs function synergistically with remdesivir to inhibit SARS-CoV-2 virus replication in Vero and/or human cells.

Particularly interesting in this set is PAR, which has the strongest potency in the human cell assay (IC_{50} = 0.55 μM), strong synergy with remdesivir (synergy score + 17.3), and low cytotoxicity (CC_{50} > 100 μM) in both the Vero and human cell assays (Table S2). However, PAR only moderately inhibits PL^{pro} and does not inhibit M^{pro} . One possibility is that inhibition of virus replication by PAR could result, at least in part, from its inhibition of a third target. Inhibition of such a putative third target might also play some role in the inhibition of virus replication by the other HCV drugs.

In addition to its function in cleavage of viral polyproteins to generate crucial viral non-structural proteins, PL^{pro} also removes the ubiquitin-like ISG15 protein from viral proteins (Daczkowski et al., 2017; Lindner et al., 2007). ISG15 conjugation in infected cells results in a dominant-negative effect on the functions of viral proteins (Zhao et al., 2016); i.e., ISGlyation disrupts a wide range of viral functions. In addition, the resulting free ISG15 is secreted from infected cells and binds to the LFA-1 receptor on immune cells, causing the release of interferon-γ and inflammatory cytokines (Swaim et al., 2017, 2020). The release of these cytokines could contribute to the strong inflammatory response, the so-called cytokine storm, that has been implicated in the severity of COVID-19 disease (McGonagle et al., 2020). Inhibition of PL^{pro} by a HCV drug should also inhibit the release of

interferon-γ and inflammatory cytokines, potentially mitigating the cytokine storm.

Viral replication assays using combinations of drugs allowed us to assess whether the interactions between HCV drugs and remdesivir are additive or synergistic. We found that these inhibitory effects are additive or synergistic depending on which HCV drug is used to inhibit virus replication. In particular, HCV drugs that inhibit PL^{pro} synergize with remdesivir to inhibit SARS-CoV-2 replication in Vero and 293T cells. These HCV drugs include SIM, VAN, GRZ, and PAR. The conclusion that inhibition of PL^{pro} alone is sufficient for synergy with remdesivir was confirmed by a combination assay with compound 6 (a GRL0617 analog) that specifically inhibits PL^{pro} but not M^{pro}. On the other hand, we show that the HCV drugs BOC and NAR that inhibit only M^{pro} have an additive rather than a synergistic interaction with remdesivir in inhibiting SARS-CoV-2 replication. The conclusion that selective inhibition of M^{pro} has an additive interaction with remdesivir was confirmed by a synergy assay with compound GC-376, that specifically inhibits M^{pro} but not PL^{pro}. Another M^{pro} inhibitor (PF-00835231) has been reported to act in combination with remdesivir, but it was not clear whether this interaction was additive or synergistic (Boras et al., 2020). It was also recently reported that SIM acts synergistically with remdesivir but that this synergy results from inhibition of M^{pro} and/or other targets (Lo et al., 2021).

The mechanism through which PL^{pro} inhibition, but not M^{pro} inhibition, results in synergy with remdesivir is not yet known. One rational mechanism involves the critical role of PL^{pro} in the formation of replication organelles (DMVs). Studies of DMV formation by SARS-CoV nsp3, nsp4, and nsp6 proteins demonstrate a requirement for all three proteins, and for a catalytically active PL^{pro} nsp3 construct (Angelini et al., 2013). HCV drugs that inhibit PL^{pro} in infected cells should therefore inhibit formation of DMVs that are required for polymerase function, reducing the amount of functional viral RNA polymerases, and hence reducing the amount of remdesivir needed for inhibition of virus replication. This hypothetical mechanism could explain why drugs that inhibit PL^{pro} (e.g., SIM, VAN, PAR, and GRZ) act synergistically with remdesivir. In contrast, the drugs that inhibit M^{pro}, but not PL^{pro} (e.g., BOC and NAR), are not synergistic with remdesivir. M^{pro} inhibitors are expected to reduce the amount of the three subunits, nsp7, nsp8, and nsp12, of the viral polymerase in infected cells. However, the reduction in the amounts of these polymerase subunits might not reduce the level of the viral polymerase sufficiently to exhibit synergy with remdesivir if there is relatively large pool of these subunits in infected cells. While M^{pro} also generates the nsp4 and nsp6 proteins that contribute to DMV formation (Angelini et al., 2013), it is not known whether this function of M^{pro} is required for DMV formation.

Synergy between PL^{pro} and viral polymerase inhibitors could also involve other viral or host targets of these protease inhibitors. Removal of ISG15 from viral or host proteins by PL^{pro} could potentially restore their functions, and inhibition of the de-ISGlyaton function of PL^{pro} could provide another mechanism for synergy between inhibitors of PL^{pro} and inhibitors of other viral or host protein functions, including remdesivir.

HCV drugs that are strongly synergistic with remdesivir are most pertinent for the goal of the present study. Repurposed drugs may not have sufficient inhibitory activity on their own to achieve clinical efficacy. Synergy with remdesivir increases the potency of both the proposed repurposed HCV drugs and remdesivir. We identified four HCV drugs, SIM, VAN, PAR, and GRZ, that act synergistically with remdesivir to inhibit SARS-CoV-2 virus replication. Of these four, SIM, PAR, and VAN are particularly interesting as repurposed drugs because they effectively inhibit SARS-CoV-2 virus replication in human cells at lower concentrations than GRZ. Consequently, the combination of an FDA-approved PL^{pro} inhibitor, such as SIM or PAR, and remdesivir, could potentially function as an antiviral against SARS-CoV-2, while more specific and potent SARS-CoV-2 antivirals are being developed. SIM, VAN, PAR, and GRZ are orally administered drugs that might also be combined with an oral polymerase inhibitor rather than with remdesivir, which has to be administered intravenously. One such oral polymerase inhibitor, molnupiravir (MK-4482) (Sheahan et al., 2020), which is currently in late-stage clinical trials, could potentially be combined with one of these four HCV protease inhibitors for clinical applications. For example, a combination of SIM and molnupiravir could be assessed for outpatient use. Beyond the proposed repurposing of these FDA-approved HCV inhibitors as antivirals for COVID-19, our results indicate that the SARS-CoV-2 PL^{pro} is an important target for future antiviral drug development that when used in conjunction with polymerase inhibitors could provide potent efficacy and protection from SARS-CoV-2, especially for virus variants that are resistant to vaccine-generated antibodies.

STAR★METHODS

Detailed methods are provided in the online version of this paper and include the following:

- KEY RESOURCES TABLE
- RESOURCE AVAILABILITY
  - Lead contact
  - Materials availability
  - Data and code availability
- EXPERIMENTAL MODELS AND SUBJECT DETAILS
- METHOD DETAILS
  - Molecular docking
  - M^{pro} expression and purification
  - M^{pro} proteolysis inhibition assays
  - M^{pro} FRET Assay
  - M^{pro} NMR Assay
  - Amide ^{1}H and ^{15}N chemical shift assignments for M^{pro} peptide substrate
  - PL^{pro} proteolysis inhibition assay
  - Cells and viruses
  - Viral growth and cytotoxicity assays in the presence of inhibitors
  - Antiviral combination assay
- QUANTIFICATION AND STATISTICAL ANALYSIS

SUPPLEMENTAL INFORMATION

Supplemental information can be found online at https://doi.org/10.1016/j.celrep.2021.109133.

ACKNOWLEDGMENTS

We thank Drs. Y.P. Huang, G. Liu, L. Ma, S. Shukla, G.V.T. Swapna, and R. Xiao for helpful discussions and comments on the manuscript. We also thank J. Hunt and S. Krishna for a generous gift of SARS-CoV-2 PL^{pro} enzyme and R. Albrecht for support with the BSL3 facility at the Icahn School of Medicine at Mount Sinai. This research was supported by grants from the National Institutes of Health (R01-GM120574 to G.T.M.) and RPI Center for Computational Innovations (to K.B. and G.T.M.). This research was also partly funded by CRIP (Center for Research for Influenza Pathogenesis), a NIAID-supported Center of Excellence for Influenza Research and Surveillance (HHSN272201400008C), DARPA grant HR0011-19-2-0020, NIAID grants U19AI142733 and U19AI135972, DOD grant W81XWH-20-1-0270, and by the generous support of the JPB Foundation, the Open Philanthropy Project (2020-215611 [5384]), and anonymous donors to A.G.-S.

AUTHOR CONTRIBUTIONS

Conceptualization, K.B., K.W., B.H., C.A.R., A.G.-S., R.M.K., and G.T.M.; methodology, K.B., K.W., B.H., T.B.A., T.R., R.R., C.A.R., A.G.-S., R.M.K., and G.T.M.; validation, K.B., K.W., B.H., C.A.R., A.G.-S., R.M.K., and G.T.M.; formal analysis, K.B., K.W., B.H., T.R., C.A.R., A.G.-S., R.M.K., and G.T.M.; investigation, K.B., K.W., B.H., R.R., T.R., E.M., T.K., and L.M.; resources, C.A.R., A.G.-S., and G.T.M.; writing – original draft, K.B., K.W., A.G.-S., R.M.K., and G.T.M.; writing, review, and editing, K.B., K.W., B.H., C.A.R., A.G.-S., R.M.K., and G.T.M.; visualization, K.B., K.W., B.H., C.A.R., A.G.-S., R.M.K., and G.T.M.; supervision, K.W., C.A.R., A.G.-S., and G.T.M.; funding acquisition, C.A.R., A.G.-S., and G.T.M.

DECLARATION OF INTERESTS

A provisional patent application related to these studies has been filed. G.T.M. is a founder of Nexomics Biosciences, Inc. The A.G.-S. laboratory has received research support from Pfizer, Senhwa Biosciences, 7Hills Pharma, Avimex, Blade Therapeutics, Dynavax, ImmunityBio, Nanocomposix, Pharmamar, and Kenall Manufacturing, and A.G.-S. has consulting agreements for the following companies involving cash and/or stock: Vivaldi Biosciences, Pagoda, Contrafect, 7Hills Pharma, Avimex, Vaxalto, Accurius, Pfizer, and Esperovax. These relationships have no conflict of interest with respect to this study.

Received: November 16, 2020
Revised: March 18, 2021
Accepted: April 23, 2021
Published: May 18, 2021

REFERENCES

Amanat, F., White, K.M., Miorin, L., Strohmeier, S., McMahon, M., Meade, P., Liu, W.C., Albrecht, R.A., Simon, V., Martinez-Sobrido, L., et al. (2020). An In Vitro Microneutralization Assay for SARS-CoV-2 Serology and Drug Screening. Curr. Protoc. Microbiol. *58*, e108.

Anand, K., Palm, G.J., Mesters, J.R., Siddell, S.G., Ziebuhr, J., and Hilgenfeld, R. (2002). Structure of coronavirus main proteinase reveals combination of a chymotrypsin fold with an extra α-helical domain. EMBO J. *21*, 3213–3224.

Angelini, M.M., Akhlaghpour, M., Neuman, B.W., and Buchmeier, M.J. (2013). Severe acute respiratory syndrome coronavirus nonstructural proteins 3, 4, and 6 induce double-membrane vesicles. MBio *4*, e00524-13.

Anson, B., and Mesecar, A. (2020). X-ray structure of SARS-CoV-2 main protease bound to boceprevir at 1.45 A. PDB ID 6WNP, Published online April 23, 2020. https://doi.org/10.2210/pdb6WNP/pdb.

Anson, B., Chapman, M., Lendy, E., Pshenychnyi, S., Richard, T., Satchell, K., and Mesecar, D.A. (2020). Broad-spectrum inhibition of coronavirus main and papain-like proteases by HCV drugs, Published online May 1, 2020. https://doi.org/10.21203/rs.3.rs-26344/v1.

Bafna, K., Krug, R.M., and Montelione, G.T. (2020). Structural similarity of SARS-CoV2 M(pro) and HCV NS3/4A proteases suggests new approaches for identifying existing drugs useful as COVID-19 therapeutics, Published online April 21, 2020. https://doi.org/10.26434/chemrxiv.12153615.

Boras, B., Jones, R.M., Anson, B.J., Arenson, D., Aschenbrenner, L., Bakowski, M.A., Beutler, N., Binder, J., Chen, E., Eng, H., et al. https://doi.org/10.1101/2020.09.12.293498.

Daczkowski, C.M., Dzimianski, J.V., Clasman, J.R., Goodwin, O., Mesecar, A.D., and Pegan, S.D. (2017). Structural Insights into the Interaction of Coronavirus Papain-Like Proteases and Interferon-Stimulated Gene Product 15 from Different Species. J. Mol. Biol. *429*, 1661–1683.

DeLano, W.L. (2009). The PyMOL Molecular Graphics System, Version 1.2r3pre (Schrödinger, LLC).

Eastman, R.T., Roth, J.S., Brimacombe, K.R., Simeonov, A., Shen, M., Patnaik, S., and Hall, M.D. (2020). Remdesivir: A Review of Its Discovery and Development Leading to Emergency Use Authorization for Treatment of COVID-19. ACS Cent. Sci. *6*, 672–683.

Forli, S., Huey, R., Pique, M.E., Sanner, M.F., Goodsell, D.S., and Olson, A.J. (2016). Computational protein-ligand docking and virtual drug screening with the AutoDock suite. Nat. Protoc. *11*, 905–919.

Fu, Z., and Huang, H. (2020). SARS CoV-2 PLpro in complex with GRL0617, PDB: 7CJM. https://doi.org/10.2210/pdb7CJM/pdb.

Fu, L., Ye, F., Feng, Y., Yu, F., Wang, Q., Wu, Y., Zhao, C., Sun, H., Huang, B., Niu, P., et al. (2020). Both Boceprevir and GC376 efficaciously inhibit SARS-CoV-2 by targeting its main protease. Nat. Commun. *11*, 4417.

Gorbalenya, A.E., Koonin, E.V., Donchenko, A.P., and Blinov, V.M. (1989). Coronavirus genome: prediction of putative functional domains in the non-structural polyprotein by comparative amino acid sequence analysis. Nucleic Acids Res. *17*, 4847–4861.

Gordon, D.E., Jang, G.M., Bouhaddou, M., Xu, J., Obernier, K., White, K.M., O'Meara, M.J., Rezelj, V.V., Guo, J.Z., Swaney, D.L., et al. (2020). A SARS-CoV-2 protein interaction map reveals targets for drug repurposing. Nature *583*, 459–468.

Gosert, R., Kanjanahaluethai, A., Egger, D., Bienz, K., and Baker, S.C. (2002). RNA replication of mouse hepatitis virus takes place at double-membrane vesicles. J. Virol. *76*, 3697–3708.

Grum-Tokars, V., Ratia, K., Begaye, A., Baker, S.C., and Mesecar, A.D. (2008). Evaluating the 3C-like protease activity of SARS-Coronavirus: recommendations for standardized assays for drug discovery. Virus Res. *133*, 63–73.

Harcourt, B.H., Jukneliene, D., Kanjanahaluethai, A., Bechill, J., Severson, K.M., Smith, C.M., Rota, P.A., and Baker, S.C. (2004). Identification of severe acute respiratory syndrome coronavirus replicase products and characterization of papain-like protease activity. J. Virol. *78*, 13600–13612.

Holm, L., and Sander, C. (1993). Protein structure comparison by alignment of distance matrices. J. Mol. Biol. *233*, 123–138.

Holm, L., and Sander, C. (1999). Protein folds and families: sequence and structure alignments. Nucleic Acids Res. *27*, 244–247.

Hung, H.C., Ke, Y.Y., Huang, S.Y., Huang, P.N., Kung, Y.A., Chang, T.Y., Yen, K.J., Peng, T.T., Chang, S.E., Huang, C.T., et al. (2020). Discovery of M Protease Inhibitors Encoded by SARS-CoV-2. Antimicrob. Agents Chemother. *64*, e00872-20.

Ianevski, A., Giri, A.K., and Aittokallio, T. (2020). SynergyFinder 2.0: visual analytics of multi-drug combination synergies. Nucleic Acids Res. *48* (*W1*), W488–W493.

Jin, Z., Du, X., Xu, Y., Deng, Y., Liu, M., Zhao, Y., Zhang, B., Li, X., Zhang, L., Peng, C., et al. (2020). Structure of M^{pro} from SARS-CoV-2 and discovery of its inhibitors. Nature *582*, 289–293.

Kasparek, A., and Smyk, B. (2018). A new approach to the old problem: Inner filter effect type I and II in fluorescence. Spectrochim. Acta A Mol. Biomol. Spectrosc. *198*, 297–303.

Kneller, D.W., Galanie, S., Phillips, G., O'Neill, H.M., Coates, L., and Kovalevsky, A. (2020a). Malleability of the SARS-CoV-2 3CL M^{pro} Active-Site Cavity Facilitates Binding of Clinical Antivirals. Structure *28*, 1313–1320.

Kneller, D.W., Phillips, G., O'Neill, H.M., Tan, K., Joachimiak, A., Coates, L., and Kovalevsky, A. (2020b). Room-temperature X-ray crystallography reveals the oxidation and reactivity of cysteine residues in SARS-CoV-2 3CL M^{pro}: insights into enzyme mechanism and drug design. IUCrJ *7*, 1028–1035.

Kolb, P., and Irwin, J.J. (2009). Docking screens: right for the right reasons? Curr. Top. Med. Chem. *9*, 755–770.

Kolb, P., Ferreira, R.S., Irwin, J.J., and Shoichet, B.K. (2009). Docking and chemoinformatic screens for new ligands and targets. Curr. Opin. Biotechnol. *20*, 429–436.

Lindner, H.A., Lytvyn, V., Qi, H., Lachance, P., Ziomek, E., and Ménard, R. (2007). Selectivity in ISG15 and ubiquitin recognition by the SARS coronavirus papain-like protease. Arch. Biochem. Biophys. *466*, 8–14.

Lo, H.S., Hui, K.P.Y., Lai, H.-M., Khan, K.S., Kaur, S., Huang, J., Li, Z., Chan, A.K.N., Cheung, H.H.-Y., Ng, K.-C., et al. (2021). Simeprevir potently suppresses SARS-CoV-2 replication and synergizes with remdesivir. ACS Cent. Sci. Published online April 15, 2021. https://doi.org/10.1021/acscentsci.0c01186.

Ma, C., Sacco, M.D., Hurst, B., Townsend, J.A., Hu, Y., Szeto, T., Zhang, X., Tarbet, B., Marty, M.T., Chen, Y., and Wang, J. (2020). Boceprevir, GC-376, and calpain inhibitors II, XII inhibit SARS-CoV-2 viral replication by targeting the viral main protease. Cell Res. *30*, 678–692.

McGonagle, D., Sharif, K., O'Regan, A., and Bridgewood, C. (2020). The Role of Cytokines including Interleukin-6 in COVID-19 induced Pneumonia and Macrophage Activation Syndrome-Like Disease. Autoimmun. Rev. *19*, 102537.

Morris, G.M., Goodsell, D.S., Halliday, R.S., Huey, R., Hart, W.E., Belew, R.K., and Olson, A.J. (1998). Automated docking using a Lamarckian genetic algorithm and an empirical binding free energy function. J. Comput. Chem. *19*, 1639–1662.

Morris, G.M., Huey, R., Lindstrom, W., Sanner, M.F., Belew, R.K., Goodsell, D.S., and Olson, A.J. (2009). AutoDock4 and AutoDockTools4: Automated docking with selective receptor flexibility. J. Comput. Chem. *30*, 2785–2791.

Osipiuk, J., Azizi, S.A., Dvorkin, S., Endres, M., Jedrzejczak, R., Jones, K.A., Kang, S., Kathayat, R.S., Kim, Y., Lisnyak, V.G., et al. (2021). Structure of papain-like protease from SARS-CoV-2 and its complexes with non-covalent inhibitors. Nat. Commun. *12*, 743.

Oudshoorn, D., Rijs, K., Limpens, R.W.A.L., Groen, K., Koster, A.J., Snijder, E.J., Kikkert, M., and Bárcena, M. (2017). Expression and Cleavage of Middle East Respiratory Syndrome Coronavirus nsp3-4 Polyprotein Induce the Formation of Double-Membrane Vesicles That Mimic Those Associated with Coronaviral RNA Replication. MBio *8*, e01658-17.

Özen, A., Prachanronarong, K., Matthew, A.N., Soumana, D.I., and Schiffer, C.A. (2019). Resistance outside the substrate envelope: hepatitis C NS3/4A protease inhibitors. Crit. Rev. Biochem. Mol. Biol. *54*, 11–26.

Pan, H., Peto, R., Abdool Karim, Q., Alejandria, M., Henao-Restrepo, A.M., Hernández García, C., Kieny, M.-P., Malekzadeh, R., Murthy, S., Preziosi, M.-P., et al. (2020). Repurposed antiviral drugs for COVID-19 – interim WHO SOLIDARITY trial results. MedRciv. https://doi.org/10.1101/2020.10.15.20209817.

Peng, Q., Peng, R., Yuan, B., Zhao, J., Wang, M., Wang, X., Wang, Q., Sun, Y., Fan, Z., Qi, J., et al. (2020). Structural and Biochemical Characterization of the nsp12-nsp7-nsp8 Core Polymerase Complex from SARS-CoV-2. Cell Rep. *31*, 107774.

Prongay, A.J., Guo, Z., Yao, N., Pichardo, J., Fischmann, T., Strickland, C., Myers, J., Jr., Weber, P.C., Beyer, B.M., Ingram, R., et al. (2007). Discovery of the HCV NS3/4A protease inhibitor (1R,5S)-N-[3-amino-1-(cyclobutylmethyl)-2,3-dioxopropyl]-3- [2(S)-[[[(1,1-dimethylethyl)amino]carbonyl]amino]-3,3-dimethyl-1-oxobutyl]- 6,6-dimethyl-3-azabicyclo[3.1.0]hexan-2(S)-carboxamide (Sch 503034) II. Key steps in structure-based optimization. J. Med. Chem. *50*, 2310–2318.

Ratia, K., Pegan, S., Takayama, J., Sleeman, K., Coughlin, M., Baliji, S., Chaudhuri, R., Fu, W., Prabhakar, B.S., Johnson, M.E., et al. (2008). A noncovalent class of papain-like protease/deubiquitinase inhibitors blocks SARS virus replication. Proc. Natl. Acad. Sci. USA *105*, 16119–16124.

Sacco, M.D., Ma, C., Lagarias, P., Gao, A., Townsend, J.A., Meng, X., Dube, P., Zhang, X., Hu, Y., Kitamura, N., et al. (2020). Structure and inhibition of the SARS-CoV-2 main protease reveal strategy for developing dual inhibitors against M^{pro} and cathepsin L. Sci. Adv. *6*, eabe0751.

Salentin, S., Schreiber, S., Haupt, V.J., Adasme, M.F., and Schroeder, M. (2015). PLIP: fully automated protein-ligand interaction profiler. Nucleic Acids Res. *43* (*W1*), W443–W447.

Sanner, M.F. (1999). Python: a programming language for software integration and development. J. Mol. Graph. Model. *17*, 57–61.

Sheahan, T.P., Sims, A.C., Zhou, S., Graham, R.L., Pruijssers, A.J., Agostini, M.L., Leist, S.R., Schäfer, A., Dinnon, K.H., 3rd, Stevens, L.J., et al. (2020). An orally bioavailable broad-spectrum antiviral inhibits SARS-CoV-2 in human airway epithelial cell cultures and multiple coronaviruses in mice. Sci. Transl. Med. *12*, eabb5883.

Snijder, E.J., Limpens, R.W.A.L., de Wilde, A.H., de Jong, A.W.M., Zevenhoven-Dobbe, J.C., Maier, H.J., Faas, F.F.G.A., Koster, A.J., and Bárcena, M. (2020). A unifying structural and functional model of the coronavirus replication organelle: Tracking down RNA synthesis. PLoS Biol. *18*, e3000715.

Swaim, C.D., Scott, A.F., Canadeo, L.A., and Huibregtse, J.M. (2017). Extracellular ISG15 Signals Cytokine Secretion through the LFA-1 Integrin Receptor. Mol. Cell *68*, 581–590.

Swaim, C.D., Canadeo, L.A., Monte, K.J., Khanna, S., Lenschow, D.J., and Huibregtse, J.M. (2020). Modulation of Extracellular ISG15 Signaling by Pathogens and Viral Effector Proteins. Cell Rep. *31*, 107772.

Wolff, G., Limpens, R.W.A.L., Zevenhoven-Dobbe, J.C., Laugks, U., Zheng, S., de Jong, A.W.M., Koning, R.I., Agard, D.A., Grünewald, K., Koster, A.J., et al. (2020a). A molecular pore spans the double membrane of the coronavirus replication organelle. Science *369*, 1395–1398.

Wolff, G., Melia, C.E., Snijder, E.J., and Bárcena, M. (2020b). Double-Membrane Vesicles as Platforms for Viral Replication. Trends Microbiol. *28*, 1022–1033.

Wu, F., Zhao, S., Yu, B., Chen, Y.M., Wang, W., Song, Z.G., Hu, Y., Tao, Z.W., Tian, J.H., Pei, Y.Y., et al. (2020). A new coronavirus associated with human respiratory disease in China. Nature *579*, 265–269.

Zhang, L., Lin, D., Kusov, Y., Nian, Y., Ma, Q., Wang, J., von Brunn, A., Leyssen, P., Lanko, K., Neyts, J., et al. (2020a). α-Ketoamides as Broad-Spectrum Inhibitors of Coronavirus and Enterovirus Replication: Structure-Based Design, Synthesis, and Activity Assessment. J. Med. Chem. *63*, 4562–4578.

Zhang, L., Lin, D., Sun, X., Curth, U., Drosten, C., Sauerhering, L., Becker, S., Rox, K., and Hilgenfeld, R. (2020b). Crystal structure of SARS-CoV-2 main protease provides a basis for design of improved α-ketoamide inhibitors. Science *368*, 409–412.

Zhao, C., Sridharan, H., Chen, R., Baker, D.P., Wang, S., and Krug, R.M. (2016). Influenza B virus non-structural protein 1 counteracts ISG15 antiviral activity by sequestering ISGylated viral proteins. Nat. Commun. *7*, 12754.

STAR★METHODS

KEY RESOURCES TABLE

REAGENT or RESOURCE	SOURCE	IDENTIFIER
Antibodies		
Anti-N protein	Dr. Thomas Moran (MSSM)	mAb 1C7
Bacterial and virus strains		
USA-WA1/2020	BEI Resources	NR-52281
Biological samples		
Not applicable		
Chemicals, peptides, and recombinant proteins		
Recombinant SARS-CoV-2 PL^{pro} protein; residues 1564 to 1881 of the SARS-CoV-2 replicase polyprotein 1a (Uniprot id P0DTD1 (R1A_SARS2)), with a C-terminal purification tag LEHHHHHH	Laboratory of Prof. J. Hunt, Columbia University	N/A
KTSAVLQ/SGFRKME NMR assay substrate	GenScript Inc; custom synthesis this paper	N/A
Dabcyl-KTSAVLQ/SGFRKME-Edans FRET assay substrate	GenScript Inc; custom synthesis this paper	N/A
zRLRGG/AMC Fluorescence assay substate	Bachem America Inc.	Cat# 4027158.0025
Ampicillin	Research Products International	Cat# A40040
IPTG	Research Products International	Cat# 156000
asunaprevir HCV protease inhibitor	Selleckchem Inc.	Cat# S4935
boceprevir HCV protease inhibitor	Selleckchem Inc.	Cat# S3733
danoprevir HCV protease inhibitor	Selleckchem Inc.	Cat# S1183
glecaprevir HCV protease inhibitor	Selleckchem Inc.	Cat# S5720
grazoprevir HCV protease inhibitor	Selleckchem Inc.	Cat# S3728
paritaprevir HCV protease inhibitor	Selleckchem Inc.	Cat# S5404
simeprevir HCV protease inhibitor	Selleckchem Inc.	Cat# S5015
telaprevir HCV protease inhibitor	Selleckchem Inc.	Cat# S1538
narlaprevir HCV protease inhibitor	MedChemExpress	Cat# HY-10300
vaniprevir HCV protease inhibitor	Addoq	Cat# A11600-5
GC-376	Selleckchem Inc.	Cat# S0457
compound 6 (GRL0617 analog)	MedChemExpress	Cat# HY-17542
remdesivir	Medkoo Bioscience Inc.	Cat# 329511
Critical commercial assays		
Not applicable		
Deposited data		
^{1}H and ^{15}N assignments for 14-residues peptide that is cleaved by SARS-CoV-2 M^{pro}.	This paper.	BioMagResDB accession number: 50568
^{1}H and ^{15}N assignments for 14-residue peptide after cleavage by SARS-CoV-2 M^{pro}	This paper	BioMagResDB accession number: 50569
Experimental models: Cell lines		
E. coli BL21(DE3)	New England Biolabs Inc	Cat# C2527
Vero E6 cells	ATCC	Cat# CRL-1586

(*Continued on next page*)

Continued

REAGENT or RESOURCE	SOURCE	IDENTIFIER
HEK293T cells	ATCC	Cat# CRL-3216
HEK293T cells transduced with a lentiviral vector expressing human ACE2. Cells were puromycin selected and then single-cell-cloned and screened for their ability to support SARS-CoV-2 replication.	This paper	
Experimental models: Organisms/strains		
Not applicable		
Oligonucleotides		
Not applicable		
Recombinant DNA		
M^{pro} expression vector GTM_COV2_NSP5_001, corresponding to residues 3264 to 3567 of the SARS-CoV-2 replicase polyprotein 1a (Uniprot id P0DTD1 (R1AB_SARS2) cloned into the pGEX-6P-1 vector with a C-terminal His_6 tag,	GenScript Inc; custom synthesis this paper	N/A
Software and algorithms		
Topspin 3.2.6	Bruker Biospin, Inc.	https://www.bruker.com/en.html
AutoDock 4.2	Morris et al., 2009	http://autodock.scripps.edu/
AutoDockTools 1.5.6	Sanner, 1999	http://autodock.scripps.edu/resources/adt
Synergy Finder	Ianevski et al., 2020	https://synergyfinder.fimm.fi/
DALI structure alignment server	Holm and Sander, 1993, 1999	http://ekhidna2.biocenter.helsinki.fi/dali/
Prism 8 graphing software	GraphPad, Inc.	https://www.graphpad.com/
Other		
Bruker Avance II 600 MHz NMR System	Bruker Biospin, Inc.	https://www.bruker.com/en.html
Infinite M1000 TECAN plate reader fluorimeter	ThermoFisher Scientific. Inc.	https://www.tecan.com/hubfs/Tecan_Journal/200801/Tecan_Journal_01_08_page16-17.pdf

RESOURCE AVAILABILITY

Lead contact

Further information and requests for resources and reagents should be directed to and will be fulfilled by the designated contact, Gaetano T. Montelione (monteg3@rpi.edu).

Materials availability

All materials generated in this study are available upon request.

Data and code availability

The following datasets generated during this study are available at the BioMagResDB:

BioMagResDB accession number: 50568. Title: "^{1}H and ^{15}N assignments for 14-residues peptide that is cleaved by SARS-CoV-2 M^{pro}." DOI: 10.13018/BMR50568
BioMagResDB accession number: 50569. Title: "^{1}H and ^{15}N assignments for 14-residue peptide after cleavage by SARS-CoV-2 $M^{pro.}$" DOI: 10.13018/BMR50569

EXPERIMENTAL MODELS AND SUBJECT DETAILS

Vero E6 (ATCC, CRL-1586) and 293T cells (ATCC, CRL-3216; kind gift of Dr. Viviana Simon), were maintained in DMEM (Corning) supplemented with 10% FB (Peak Serum) and penicillin/streptomycin (Corning) at 37°C and 5% CO_2. hACE2-293T cells were generated for this study. Briefly, 293T cells were transduced with a lentiviral vector expressing human ACE2. Puromycin resistant cells with

hACE2 surface expression were sorted after staining with AlexaFluor 647-conjugated goat anti-hACE2 antibodies. Cells were then single-cell-cloned and screened for their ability to support SARS-CoV-2 replication. All cell lines used in this study were regularly screened for mycoplasma contamination using the Universal Detection Kit (ATCC, 30-1012K).

METHOD DETAILS

Molecular docking

We used the free open source *AutoDock* suite (Morris et al., 2009). *AutoDockTools* (Sanner, 1999) was used for coordinate preparation, docking, and analysis of results. The computational docking program *AutoDock v4.2.6*. is based on an empirical free-energy force field and uses a search method based on Lamarckian genetic algorithm (Morris et al., 1998). Target protein coordinates were obtained from SARS-CoV-2 M^{pro} X-ray crystal structure (PDB id 6Y2G) (Zhang et al., 2020b), and structural water was removed. Three-dimensional coordinates for ligand molecules were obtained from PDB (http://www.rcsb.org/) or from chemical structure databases, ChemSpider (http://www.chemspider.com/) and DrugBank (https://go.drugbank.com/). Protein and ligand coordinates were prepared using *AutoDockTools*; polar hydrogens were added to protein structures, and Gasteiger-Marsili empirical atomic partial charges were added to ligands. Torsional degrees of freedom (dihedral angles) were identified for each ligand. These data and parameters for each protein and ligand were saved as individual PDBQT files. In these studies, ligand dihedral angles were allowed to vary (except where stated otherwise), and all protein dihedral angles were kept rigid. The program *Autogrid* (Sanner, 1999) was used to prepare affinity maps for all atom types in the receptor and ligands. A grid of 56, 40 and 48 points in x, y, and z direction, with a grid spacing of 0.375 Å was used to compute electrostatic maps. The grid center was placed on the center of the inhibitor 13b molecule in its complex with M^{pro} (PDB id 6Y2G) (Zhang et al., 2020b). The Lamarckian genetic algorithm (LGA) method was used for sampling ligand binding conformation (Morris et al., 1998), with the following LGA parameters: 150 individuals in population; 2,500,000 energy evaluations; 27,000 maximum number of generations; and with mutation and crossover rates of 0.02 and 0.08, respectively. A maximum of 300 iterations per local search was used. The calculations were repeated for 100 docking simulations for each HCV drug. All docking simulations were analyzed using the *AutoDockTools.* Atomic coordinates for best scoring conformation obtained in each docking simulation, for each drug-protein complex, were saved in PDB format for analysis. In addition, because the experimentally-determined pose is often not the one with the lowest docking energy, but rather is found among other highly-ranked poses (Kolb et al., 2009; Kolb and Irwin, 2009), we also examined other low-energy poses. These protein-ligand complexes were analyzed in detailed using open source *PyMol* molecular visualization tool (DeLano, 2009) and fully automated *Protein-Ligand Interaction Profiler* (Salentin et al., 2015) (https://plip-tool.biotec.tu-dresden.de/plip-web/plip/index).

For a comparative analysis, docking simulations of the α-ketoamide inhibitor 13b (Zhang et al., 2020b) were also performed using the same protocol used for docking HCV protease inhibitor drugs. In the 1.75-Å X-ray crystal structure of the 13b-M^{pro} complex (Zhang et al., 2020b), 13b makes hydrogen-bonded interactions with backbone amides of key residues, Gly143, Ser144 and Cys145, in the canonical oxyanion hole of the active site. To estimate the docking score for the pose observed in this X-ray crystal structure, we first carried out docking using a modified protocol in which the dihedral angles of 13b were fixed to the values observed in the crystal structure. The lowest energy pose obtained with this protocol matches the crystal structure almost exactly (Figure S1B), with *AutoDock* binding energy of −7.19 kcal/mol. Next, we assessed the docking protocol using flexible ligand dihedral angles, as was used for all the HCV protease inhibitors. The best-scoring docked conformation (Figure S1C), has an *AutoDock* binding energy of −9.17 kcal/mol. A pose with slightly higher binding energy of −9.03 kcal/mol, is almost identical to the pose observed in the crystal structure (Figure S1D). Hence, binding poses very similar to that observed in the crystal structure are indeed included among the low energy poses generated by the *AutoDock* protocol.

For PL^{pro}, inhibitor complexes in the PDB revealed that the BL2 loop present at the entrance of active site adopts significantly different conformations depending on the size of the inhibitor bound to the PL^{pro} . This plasticity in the BL2 loop suggests an induced fit mechanism of ligand binding to PL^{pro} active site. To avoid a closed conformation of the BL2 loop found in protein ligand complex we chose a SARS-CoV-2 PL^{pro} X-ray crystal structure in its apo form (PDB id 6W9C) as the target to dock HCV protease inhibitors. The docking protocol was same as above, except a larger grid of size 56, 56, and 58 points in the x, y, and z direction respectively was used to compute electrostatic maps for PL^{pro} target. For a comparative analysis, docking simulations of PL^{pro} inhibitor GRL0617 (PDB id 7CJM) were also performed using the same protocol.

M^{pro} expression and purification

The full-length SARS-CoV-2 M^{pro} gene, corresponding to residues 3264 to 3567 of the SARS-CoV-2 replicase polyprotein 1a [Uniprot id P0DTD1 (R1AB_SARS2)], was obtained from GenScript USA, Inc. and cloned into the pGEX-6P-1 vector with a C-terminal His_6 tag, as previously described (Zhang et al., 2020b). This expression vector is designated GTM_COV2_NSP5_001. This plasmid, which expresses SARS-CoV-2 M^{pro} as a self-cleaving (using its native cleavage site) GST-fusion, was transformed into competent *E. coli* BL21(DE3) cells. A single colony was picked and inoculated in 2 mL LB supplemented with 0.1 mg/ml ampicillin at 37°C and 225 rpm. The 2 mL inoculum was added to 1L LB broth with 0.1 mg/mL ampicillin. The cells were allowed to grow to an optical density of 0.6 at 600 nm at 37°C and 225 rpm, and were induced with 1 mM IPTG. The induced cells were incubated overnight at 18°C and 225 rpm. The cells were harvested and resuspended in lysis buffer (20 mM Tris pH 8.0, 300 mM NaCl) and then lysed by sonication. The cell debris was removed by centrifugation at 14,000 rpm for 40 mins. The supernatant was added to a Ni-NTA

column pre-equilibrated with loading buffer (20 mM Tris pH 8.0, 300 mM NaCl, 10 mM imidazole), and bound proteins were eluted with 20 mM Tris pH 8.0, containing 100 mM NaCl and100 mM imidazole. The elution fractions that contained M^{pro} were buffer exchanged (20 mM Tris pH 8.0, 100 mM NaCl, 1 mM EDTA, 1 mM DTT) and concentrated using a swinging bucket centrifuge at 4000 rpm. The final M^{pro} concentration was 23.3 μM, determined by absorbance at 280 nm using a calculated extinction coefficient of 33,640 M^{-1} cm^{-1}. Homogeneity was validated by SDS-PAGE (> 95% homogeneous), and the construct was validated by MALDI-TOF mass spectrometry. The enzymatic activity of freshly purified M^{pro} was measured using Michealis Menten equation best fit values of K_M and V_{max}; these were 55.5 μM and 0.018 μM/sec, respectively. The calculated k_{cat} was 1.80 s^{-1}, and k_{cat}/K_M was 32,400 s^{-1} M^{-1}.

M^{pro} was observed to be unusually sensitive to active site Cys oxidation (Kneller et al., 2020b), requiring special care in preparing samples, maintaining them under reducing conditions, and checking samples for time-dependent loss of activity over the course of enzyme activity and drug inhibition measurements. Purified samples of M^{pro} were prepared in 20 mM TRIS buffer, pH 8.0, containing 100 mM NaCl, 1 mM EDTA, and 1 mM DTT, flash frozen in 50 μL aliquots, and stored at −80°For enzyme assays, freshly thawed enzyme aliquots were prepared in buffers containing 3 mM TCEP, and assayed for specific activity at the beginning and end of the data collection session, or back-to-back with each measurement, in order to avoid spurious results due to enzyme inactivation during a measurement session.

M^{pro} proteolysis inhibition assays

The proteolysis of substrate KTSAVLQ/SGFRKME was studied using Fluorescence Resonance Energy Transfer (FRET) and nuclear magnetic resonance (NMR) assays. Fluorescence studies were carried out using an Infinite M1000 TECAN plate reader, with 3 mm path lengths, and Magellan™ software. NMR assays were carried out using a Bruker Avance II 600 MHz NMR spectrometer system. For the FRET assay the substrate was Dabsyl-KTSAVLQ/SGFRKME-Edans, labeled with a Dabcyl and Edans FRET pair on the N and C-termini of the peptide, respectively, as described elsewhere (Ma et al., 2020). The NMR assay used the same peptide substrate without the fluorescence dyes attached. Both labeled and unlabeled peptide substrates were obtained from GenScript USA, Inc.

As part of our initial development of the FRET assay for M^{pro} activity, we assessed catalysis rates over the range of 1 nM to 200 nM enzyme concentration, with the fluorophore-labeled peptide substrate. We observed significant proteolytic activity over this whole range (Figure S2). As rates of hydrolysis at enzyme concentrations > ∼50 nM are quite fast, the concentration of 10 nM was selected in order to provide the most accurate kinetic data. Other FRET-based assays of M^{pro} activity have been reported using enzyme concentrations ranging from 20 nM to 500 nM (Fu et al., 2020; Grum-Tokars et al., 2008; Hung et al., 2020; Lo et al., 2021; Ma et al., 2020). However, it is well established that the kinetic properties of SARS CoV M^{pro} are significantly influenced by the construct and assay conditions utilized (Grum-Tokars et al., 2008). For SARS CoV M^{pro}, the monomeric form is inactive and dimerization is required for its enzymatic activity (Grum-Tokars et al., 2008). Reports of the dimer dissociation constant K_d for SARS-CoV M^{pro} range from 1 nM to 200 μM; these dimer dissociation constants are also very sensitive to the presence of non-native N- or C-terminal residues (Grum-Tokars et al., 2008). The dimer dissociation constant K_d for a similar construct of SARS-CoV-2 M^{pro} has been reported to be ∼2.5 μM (Zhang et al., 2020b). Hence, the fraction of active enzyme present at 10 nM concentration is expected to be quite low. However, other groups have also reported SARS-CoV-2 M^{pro} enzyme activity assays at 20 nM enzyme concentration (Hung et al., 2020). Assuming the substrate binds more tightly to the dimer than to the monomer, the thermodynamic equilibrium between monomer and dimer would be expected to be shifted by the substrate, resulting in the observed protease activity even at enzyme concentrations well below the homodimer K_d. In this case, in the right concentration range there would be a non-linear dependence of activity versus enzyme concentration. This was not observed over the range of 0 to 20 nM enzyme concentration (Figure S2). Alternatively, the monomeric form of the SARS-CoV-2 M^{pro} may in fact have significant protease activity.

M^{pro} FRET Assay

All M^{pro} protease assays were carried out in Reaction Buffer containing 20 mM HEPES pH 6.5, 120 mM NaCl, 0.4 mM EDTA and 3 mM TCEP. Additionally, 1 mg/mL BSA was added to the buffer for FRET assays. For the FRET assay, 10 nM M^{pro} was incubated with 20 μM of HCV drugs. The reaction was initiated by addition of 20 μM FRET substrate and monitored for 2 hours on an Infinite M1000 TECAN plate reader, exciting at 360 nm and detecting donor emission at 460 nm. The initial velocity of the reaction was calculated as the slope obtained from linear fits of emission intensity versus time plots for the first 15 minutes of the reaction. All FRET data were analyzed and plotted for initial velocity on Microsoft Excel.

In the FRET assays, the percent proteolytic activity in the presence of each drug was calculated as a ratio of initial velocity in presence of inhibitor (v_i) to initial velocity in absence of inhibitor (v_{i0}) i.e., v_i / v_{i0}. A histogram plot of v_i / v_{i0} for each inhibitor was used to compare relative inhibition activities. All FRET proteolysis reaction curves were measured twice, and the uncertainty in v_i / v_{i0}, estimated from the standard deviation of 2 independent measurements is shown as error bars. Short (< 3 min) time points exhibiting equilibration artifacts (Figure S2A) were excluded from this analysis.

For IC_{50} measurements of HCV inhibitors BOC, NAR and TEL, 10 nM of M^{pro} was incubated with a range of inhibitor concentrations in the same Reaction Buffer described above. The inhibitor concentration ranges were 0.1 – 200 μM for BOC, 0.1 to 100 μM for NAR, and 0.2 to 100 μM for TEL. The reaction was initiated by adding 20 μM FRET substrate and monitored for 1 hr. Each measurement was repeated three times. The percent inhibition at each inhibitor concentration was calculated as:

$$\% \text{ Inhibition} = 100 * (v_i - v_{i0})/(v_{imax} - v_0)$$

where v_i = initial velocity at a given inhibitor concentration
v_{i0} = initial velocity in absence of inhibitor
v_{imax} = initial velocity at maximum inhibition

The percent inhibition was plotted as a function of inhibitor concentration to obtain a dose-response curve using Prism 8 (GraphPad Software) software. IC_{50} was calculated from fitting to the equation:

$$\% \text{ Inhibition} = 100 * [\text{Inhibitor}] / (IC_{50} + [\text{Inhibitor}])$$

For several of the HCV drugs, intrinsic fluorescence of the drugs appears to compromise the accuracy of the FRET kinetic curves. Even though little or no inner filter effects were observed (Kasparek and Smyk, 2018) in these measurements, simple subtraction of the drug fluorescence from the final values of kinetic curves results in curves which do not match the final values for curves obtained in the absence of drugs, suggesting possible energy transfer between the drug and the FRET fluorophores on the peptide substrate.

The inner filter effect results from absorbance of the sample at the fluorescence excitation wavelength, attenuating fluorescence excitation (Kasparek and Smyk, 2018). Boceprevir, narleprevir, and telaprevir, which do not have significant intrinsic fluorescence but have similar extinction coefficients to the other drugs at 360 nm, did not present a problem for the assay, indicating that inner filter effects are not significant. The inner filter effect (Kasparek and Smyk, 2018) was experimentally assessed by measuring fluorescence and emission for the fluorescent dye diethylamino naphthalene sulfonate (DENS) over the range 0.01 to 1.0 O.D. units, at the excitation wavelength (360 nm), using the Infinite M1000 TECAN plate reader fluorimeter. These data show that in this system the inner filter effects are negligible for samples with total $OD_{360} < 0.025$, similar to results reported elsewhere (Kasparek and Smyk, 2018). As summarized in Table S3, with the exception of the vaniprevir study, these reaction mixtures had $OD_{360} < 0.025$. Hence, under the conditions of these assays, most of the assay samples have no significant inner filter effect; only the vaniprevir assay had a small effect, which was appropriately corrected for.

M^{pro} NMR Assay

For the M^{pro} ^1H NMR proteolysis assay the reaction was performed at 100 nM M^{pro} in the same assay buffer described above, along with 5% D_2O and 50 μM HCV inhibitors dissolved in d_6-DMSO. For the control experiments where no inhibitor is added, the same quantity of d_6-DMSO was added. 50 μM of unlabeled peptide substrate was added and immediately transferred to a 5-mm NMR tube. The final volume of each reaction mixture was 600 μL. The NMR tube was quickly placed in a 600 MHz Bruker Avance II spectrometer equipped with a 5-mm TCI cryoprobe, equilibrated at 298 K. The homogeneity of the magnetic field was adjusted by gradient shimming on the z axis, and in each case an array of 24 ^1H experiments was acquired with 1D ^1H NMR using excitation sculpting for water suppression. The probe had previously been tuned and matched with a sample of similar composition. The delay between initiation of the reaction and starting acquisition was ~5 mins for most of the reaction conditions. The duration of each NMR experiment was also taken into account to obtain accurate time values. All ^1H spectra were acquired, processed, and analyzed in Bruker TopSpin 3.6.2 software. The regions of interest were integrated, and the values obtained were used for further analysis and plotting.

These ^1H NMR spectra were used to monitor the evolution of substrate and product as a function of time. Resonance assignments (discussed below) of the cleaved and uncleaved KTSAVLQ/SGFRKME peptide identified the amide H^N resonances that were monitored during the reaction. The H^N resonances for amino-acid residues Phe-10 (uncleaved) and Gln-7 (cleaved) were used to quantify substrate utilization and product formation, respectively, during the reaction. The H^N peak intensity of residue Glu-14, which did not shift upon cleavage, was monitored as an internal control. The percent substrate cleavage in the presence of inhibitors at 30 min was calculated as a ratio of the H^N resonance integrals of Gln-7 in presence of inhibitor to the corresponding resonance integral with no inhibitor.

Amide ^1H and ^{15}N chemical shift assignments for M^{pro} peptide substrate

Chemical shift assignments of backbone amide ^1H and ^{15}N resonances in the 14-residue peptide KTSAVLQSGFRKME in 20 mM HEPES pH 6.5, 100 mM NaCl, 0.4 mM EDTA, 3 mM TCEP and 5% ^2H_2O were determined at 298 K using 2D COSY, TOCSY, and ^1H-^{15}N HSQC, along with 1D ^1H NMR experiments, and referenced to internal DSS. Backbone amide ^1H and ^{15}N resonances were assigned for 12/14 and 10/14 residues in the uncleaved and cleaved peptide respectively. These assignments have been deposited in the BioMagResDB as BMRB entries 50568 and 50569, respectively.

PL^{pro} proteolysis inhibition assay

SARS-CoV-2 PL^{pro} enzyme was provided as a generous gift by Prof. John Hunt (Columbia University). The construct, residues 1564 to 1881 of the SARS-CoV-2 replicase polyprotein 1a (Uniprot id P0DTD1 (R1A_SARS2)), was produced in expression vector pET21_NESG with a C-terminal purification tag LEHHHHHH. Homogeneity (> 95%) was validated by SDS-PAGE. The fluorogenic substrate zRLRGG/AMC was obtained from Bachem. All PL^{pro} proteolysis assays were carried out in buffer containing 50 mM HEPES, pH 7.5, 5 mM DTT, 1 mg/ml BSA. For the fluorescence assay, 20 nM of PL^{pro} was incubated with 20 μM of HCV drugs. 20 μM substrate was added and the reaction was monitored for 2 hr using the Infinite M1000 TECAN plate reader with Magellan ™ software, with filters for

excitation at 360 nm and emission at 460 nm. No anomalous fluorescence interactions were observed in this assay for any of the drugs. We also assessed the PL^{pro} fluorescence assay for inner filter effects. As shown in Table S3, inner filter effects were also not significant in this assay, except for the vaniprevir study for which appropriate corrections were made.

The data points for the first 10 mins of the proteolysis reaction progression curves were used to calculate the initial velocity (v_i) in the presence and absence of the inhibitor. The percent proteolytic activity in presence of each drug is calculate as a ratio of initial velocity in presence of inhibitor (v_i) to initial velocity in absence of inhibitor (v_{i0}), i.e., v_i / v_{i0}. A histogram plot of v_i / v_{i0} for each inhibitor was used to compare relative inhibition activities. All proteolysis reaction curves were measured twice, and the standard deviation (s.d.) in v_i / v_{i0} is shown as error bars.

Cells and viruses

Vero E6 (ATCC, CRL-1586) and 293T cells (ATCC, CRL-3216; kind gift of Dr. Viviana Simon), were maintained in DMEM (Corning) supplemented with 10% FB (Peak Serum) and penicillin/streptomycin (Corning) at 37°C and 5% CO_2. hACE2-293T cells were generated for this study. Briefly, 293T cells were transduced with a lentiviral vector expressing human ACE2. Puromycin resistant cells with hACE2 surface expression were sorted after staining with AlexaFluor 647-conjugated goat anti-hACE2 antibodies. Cells were then single-cell-cloned and screened for their ability to support SARS-CoV-2 replication. All cell lines used in this study were regularly screened for mycoplasma contamination using the Universal Detection Kit (ATCC, 30-1012K). Cells were infected with SARS-CoV-2, isolate USA-WA1/2020 (BEI Resources NR-52281) under biosafety level 3 (BSL3) containment in accordance to the biosafety protocols developed by the Icahn School of Medicine at Mount Sinai. Viral stocks were grown in Vero E6 cells as previously described (Amanat et al., 2020), and were validated by genome sequencing.

Viral growth and cytotoxicity assays in the presence of inhibitors

2,000 Vero E6 or hACE2-293T cells were seeded into 96-well plates in DMEM (10% FBS) and incubated for 24 h at 37C, 5% CO2. Two hours before infection, the medium was replaced with 100 μL of DMEM (2% FBS) containing the compound of interest at concentrations 50% greater than those indicated, including a DMSO control. Plates were then transferred into the BSL3 facility and 100 PFU (MOI = 0.025) was added in 50 μL of DMEM (2% FBS), bringing the final compound concentration to those indicated. Plates were then incubated for 48 h at 37°C. After infection, supernatants were removed and cells were fixed with 4% formaldehyde for 24 hours prior to being removed from the BSL3 facility. The cells were then immunostained for the viral NP protein [an in-house mAb 1C7, provided by Dr. Thomas Moran (MSSM)] with a DAPI counterstain. Infected cells (488 nM) and total cells (DAPI) were quantified using the Celigo (Nexcelcom) imaging cytometer. Infectivity was measured by the accumulation of viral NP protein in the nucleus of the Vero E6 cells (fluorescence accumulation). Percent infection was quantified as

$$[(\text{Infectedcells} / \text{Totalcells}) - \text{Background}] * 100$$

and the DMSO control was then set to 100% infection for analysis. The IC_{50} and IC_{90} for each experiment were determined using the Prism (GraphPad Software) software. Cytotoxicity was also performed using the MTT assay (Roche), according to the manufacturer's instructions. Cytotoxicity was performed in uninfected VeroE6 cells with same compound dilutions and concurrent with viral replication assay. All assays were performed in biologically independent triplicates. Remdesivir was purchased from Medkoo Bioscience inc. Time of addition experiments were performed using the same immunofluorescence-based assay with the following alterations: Vero E6 cells were infected with 8000 PFU (moi of 2) of SARS-CoV-2, the drug was added at different times relative to infection as indicated, and the infection was ended by fixation with 4% formaldehyde after 8 hours of infection (single cycle assay).

Antiviral combination assay

Like the previous antiviral assay, 2,000 Vero E6 cells were seeded into 96-well plates in DMEM (10% FBS) and incubated for 24 h at 37°C, 5% CO_2. Two hours before infection, the medium was replaced with 100 μL of DMEM (2% FBS) containing the combination of HCV protease inhibitors and remdesivir following a dilution combination matrix. A 6 by 6 matrix of drug combinations was prepared in triplicate by making serial two-fold dilutions of the drugs on each axis, including a DMSO control column and row. The resulting matrix had no drug in the right upper well, a single drug in rising 2-fold concentrations in the vertical and horizontal axes starting from that well, and the remaining wells with rising concentrations of drug mixtures reaching maximum concentrations of the drugs at the lower left well. Plates were then transferred into the BSL3 facility and SARS-CoV-2 (MOI 0.025) was added in 50 μL of DMEM (2% FBS), bringing the final compound concentration to those indicated in the figures. Plates were then incubated for 48 h at 37°C. After infection, cells were fixed with final concentration of 5% formaldehyde for 24 hours prior to being removed from the BSL3 facility. The cells were then immunostained for the viral NP protein using the in-house mAb 1C7 provided by Dr. Thomas Moran, MSSM) with a DAPI counterstain. Infected cells (AlexaFluor 488) and total cells (DAPI) were quantified using the Celigo (Nexcelcom) imaging cytometer. Infectivity was measured by the accumulation of viral NP protein in the nucleus of the Vero E6 cells (fluorescence accumulation). Percent infection was quantified as [(Infected cells/Total cells) – Background] *100, and the DMSO control was then set to 100% infection for analysis. The combination antiviral assay was performed in biologically independent triplicates.

The apparent IC_{90} for each combination in the matrix was determined using the Prism (GraphPad Software) software. The IC_{90} for HCV drugs and remdesivir were calculated for each drug treatment alone and in combination. This combination data were analyzed

using SynergyFinder by the ZIP method (Ianevski et al., 2020), and combination indices were calculated as previously described (Amanat et al., 2020).

QUANTIFICATION AND STATISTICAL ANALYSIS

Viral replication measurements were each done in triplicate (n = 3), and reported as mean ± s.d. Fluorescence measurements were done in triplicate (n = 3) or duplicate (n = 2) and reported as mean ± s.d. Estimates of uncertainties in NMR intensity measurements were determined from the spectral noise, and propagated to uncertainties in peak ratios ΔR as: $(\Delta R/R)^2 = (\Delta A/A)^2 + (\Delta B/B)^2$, where A, B, and R are the intensities of peaks A and B and their ratio, respectively, and ΔA and ΔB are the noise associated with each intensity measurement (https://nmr.chem.ucsb.edu/protocols/SNR.html).

Cell Reports, Volume *35*

Supplemental information

Hepatitis C virus drugs that inhibit SARS-CoV-2 papain-like protease synergize with remdesivir to suppress viral replication in cell culture

Khushboo Bafna, Kris White, Balasubramanian Harish, Romel Rosales, Theresa A. Ramelot, Thomas B. Acton, Elena Moreno, Thomas Kehrer, Lisa Miorin, Catherine A. Royer, Adolfo García-Sastre, Robert M. Krug, and Gaetano T. Montelione

Inhibitor	Identifier of Protease Inhibitor	Database ID of Protease Inhibitor Structure	*AutoDock* Score (kcal/mol) Lowest "Energy"	
			M^{pro}	PL^{pro}
SARS-CoV-2 M^{pro} Inhibitor				
α-ketoamide inhibitor 13b				
lowest "energy" pose	06K	6Y2G[a]	-9.17	Not Applicable
pose most similar to X-ray structure:			-9.03	
SARS-CoV-2 PL^{pro} Inhibitor				
GRL0167				
lowest "energy" pose		7CJM[a]	Not Applicable	-7.54
HCV NSP3/4A Protease Inhibitor Drugs				
vaniprevir	VAN	3SU3[c]	-10.95	-7.85
simeprevir	SIM	3KEE[c]	-10.75	-8.12
paritaprevi	PAR	32700634[b]	-10.71	-10.30
danoprevi	DAN	3M5L[c]	-9.99	-8.48
narlaprevir	NAR	3LON[c]	-9.80	-5.56
grazoprevi	GRZ	3SUD[c]	-9.71	-8.10
glecaprevir	GLE	35013015 [b]	-9.51	-8.30
boceprevir	BOC	10324367[d]	-9.13	-5.56
telaprevir	TEL	3SV6[c]	-9.05	-6.57
asunaprevir	ASU	4WF8[c]	-8.37	-6.57

Supplementary Table S1. AutoDock docking scores for SARS-CoV-2 M^{pro} and HCV NS3/4A protease inhibitors. Related to Figure panels 1A-D, Figure 6A, and STAR Methods. (a) Atomic coordinates for the inhibitor were taken from listed PDB id. (b) Atomic coordinates for the inhibitor were taken from the ChemSpider database. (c) Atomic coordinates for the inhibitor were taken from the PDB coordinates of the corresponding complex of the inhibitor bound to HCV NS3/4A protease. (d) Atomic coordinates for the inhibitor were taken from the Pubchem database.

			Vero E6 Cells		HEK 293T Cells			
	Relative M^{pro} Inhibition[a]	**Relative PL^{pro} Inhibition[a]**	**IC_{50}**	**CC_{50}**	**IC_{50}**	**CC_{50}**	**Synergy Score**	
BOC	strong	none	19.6	>50	5.4	>50	-7.6	additive
NAR	strong	none	7.7	>20	15.0	72.0	-3.6	additive
TEL	strong	none	>50	>50	20.5	>50	-	not tested
SIM	moderate	strong	4.2	2.1	2.3	>50	+30.2	synergistic
VAN	strong	strong	6.2	4.3	3.0	>50	+10.9	synergistic
PAR	none	moderate	6.0	>100	0.55	>100	+17.3	synergistic
GRZ	moderate	moderate	10.8	>50	16.7	>50	+25.0	synergistic
ASU	moderate	none	15.0	48.9	48.4	>50	-	not tested
GLE	none	none	>50	>50	>50	>50	-	not tested
DAN	none	none	>50	>50	>50	31.1	-	not tested

Supplementary Table S2. **Comparison of enzyme inhibition and viral inhibition activities of HCV protease inhibitors**. Related to Figures 1, 2, 3, 4, 5, and 6. (a) Strong inhibition corresponds to an estimated IC_{50} < about 20 μM, moderate inhibition corresponds to an estimated IC_{50} in the range 20 – 50 μM, and none indicates no observed inhibition of protease activity at drug concentrations of 50 μM.

.

Drug or Inhibitor Molecule	M^{pro} Assay		PL^{pro} Assay	
	OD_{360} of reaction mixture	Inner filter correction factor	OD_{360} of reaction mixture	Inner filter correction factor
BOC	0.0143	1.000	0.0053	1.000
NAR	0.0114	1.000	0.0024	1.000
TEL	0.0112	1.000	0.0022	1.000
SIM	0.0201	1.000	0.0111	1.000
VAN	0.0398	1.300	0.0308	1.125
PAR	0.0159	1.000	0.0068	1.000
GRZ	0.0161	1.000	0.0071	1.000
ASU	0.0197	1.000	0.0107	1.000
GLE	0.0191	1.000	0.0101	1.000
DAN	0.0126	1.000	0.0036	1.000

Supplementary Table S3. Inner filter effect corrections to fluorescence-based enzyme assays. Related to Figures 1B, 1E, 5B, 6A, and 6B, and STAR Methods. The inner filter effect was assessed by measuring fluorescence and emission for the fluorescent dye diethylamino naphthalene sulfonate (DENS) over the range 0.01 to 1.0 O.D. units, at the excitation wavelength (360 nm), using the Infinite M1000 TECAN plate reader. In this microtiter plate system, inner filter effects are negligible for A_{360} values below ~ 0.025 OD units. For each of the fluorescent peptide substrate (20 μM) / drug (20 μM) mixtures, the A_{360} was measured, and compared with fluorescence emission vs absorbance data obtained on a control fluorophore dye, DENS, to determine the inner filter effect correction value. At these peptide and drug concentrations, only the vaniprevir drug peptide mixtures required inner-filter effect corrections.

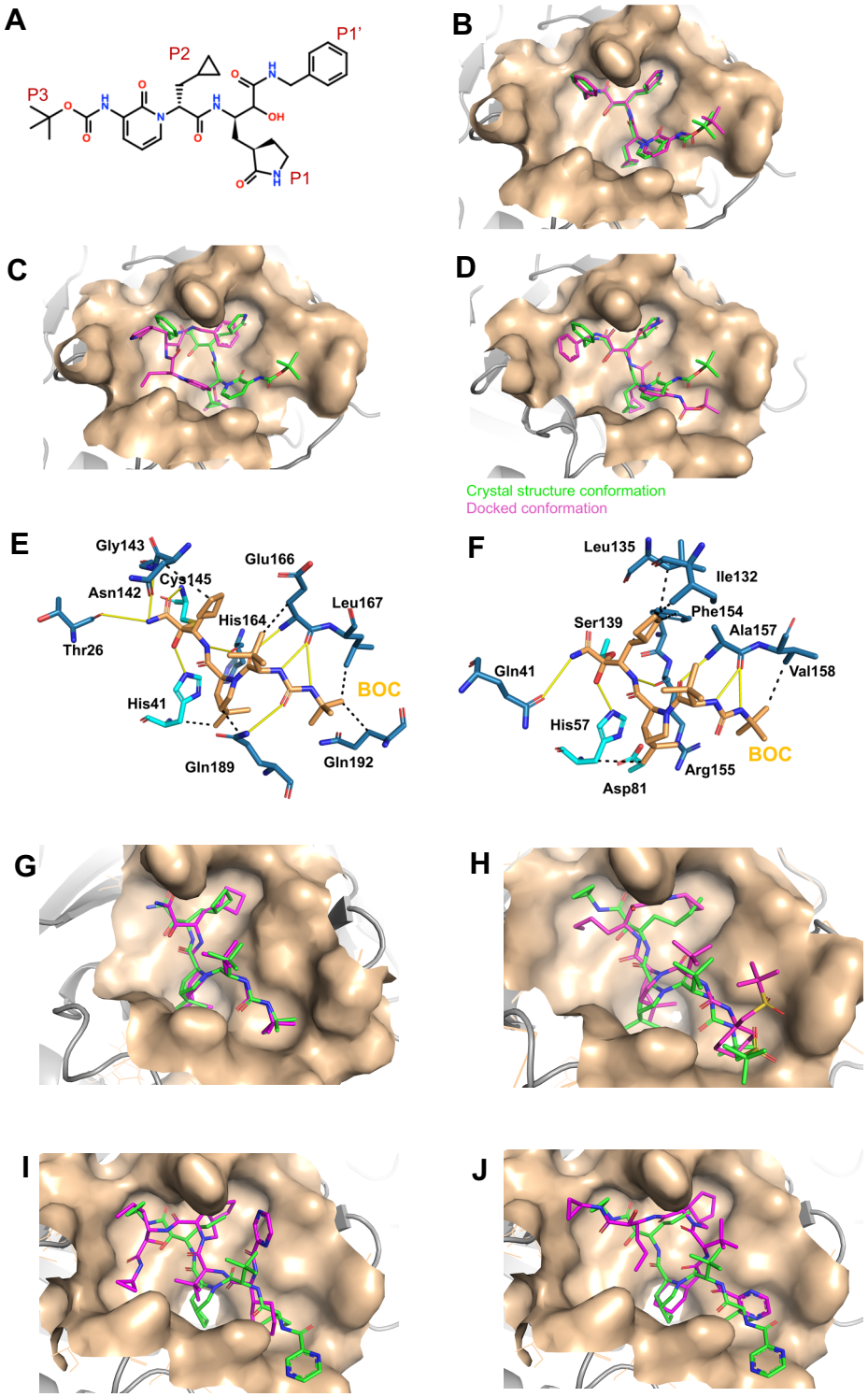

Fig. S1. Comparison of covalent inhibitor complexes of *AutoDock* with subsequently determined X-ray crystal structures. Related to Figures 1A-G, Figures 5A-B, and STAR Methods. (A) Chemical structure of α-ketoamide inhibitor 13b, in the alcohol form resulting from forming hemithioketal with Cys thiol of M^{pro} (Zhang et al., 2020b). (B) Lowest "energy" *AutoDock* pose using a rigid conformation of α-ketoamide inhibitor 13b, in order to match the ligand conformation in X-ray crystal structure of the complex (score = -7.19 kcal/mol). (C) Lowest "energy" *AutoDock* pose observed among 100 docking simulations (score = -9.17 kcal/mol). (D) The low "energy" *AutoDock* pose (score = -9.03 kcal/mol) of 13b that is most similar to the conformation seen in the crystal structure. In panels B-D, M^{pro} is shown in surface representation, X-ray crystal structure of α-ketoamide inhibitor 13b bound in the active site of M^{pro} in green sticks (PDB id 6Y2G), and the predicted *AutoDock* conformation in magenta sticks. (E) Details from the X-ray crystal

structure of the SARS-CoV-2 M^{pro} protease - boceprevir (BOC) complex [PDB id 6WNP, (Anson et al., 2020)]. (F) Details from the X-ray crystal structure of the HCV NS3/4A protease - BOC complex [(PDB id 2OC8, (Prongay et al., 2007)]. In both of these boceprevir – protease complex structures, remarkable similarity is observed between the binding poses and protein-inhibitor hydrogen bond networks. In the complex with HCV protease, boceprevir forms hydrogen bonds with side chains of residues Gln41 and His57 and with backbone atoms of Gly137, Ser139, Arg155 and Ala157. The corresponding residue equivalents (based on structural superimposition) of these residues in M^{pro}, Thr26, His41, Gly143, Cys145, His164 and Glu166, also form hydrogen bonds with boceprevir. The sidechain of residue Gln189 of SARS-CoV-2 M^{pro} forms an additional hydrogen-bond with boceprevir. (G) BOC binding pose in best-scoring *AutoDock* complex (magenta) compared with the X-ray crystal structure of a second BOC-M^{pro} complex [green, PDB id 6XQU, (Kneller et al., 2020a). (H) Narleprevir (NAR) binding pose in best-scoring *AutoDock* complex (magenta) compared with the X-ray crystal structure of the NAR-M^{pro} complex [green, PDB id 6XQT, (Kneller et al., 2020a). (I) Telaprevir (TEL) binding pose in second-best-scoring *AutoDock* complex (magenta) compared with the X-ray crystal structure of TEL-M^{pro} complex (green, PDB id 6XQS, (Kneller et al., 2020a). (J) TEL binding pose in 37th-ranked *AutoDock* complex (magenta) compared with the X-ray crystal structure of TEL-M^{pro} complex [green, PDB id 6XQS, (Kneller et al., 2020a).

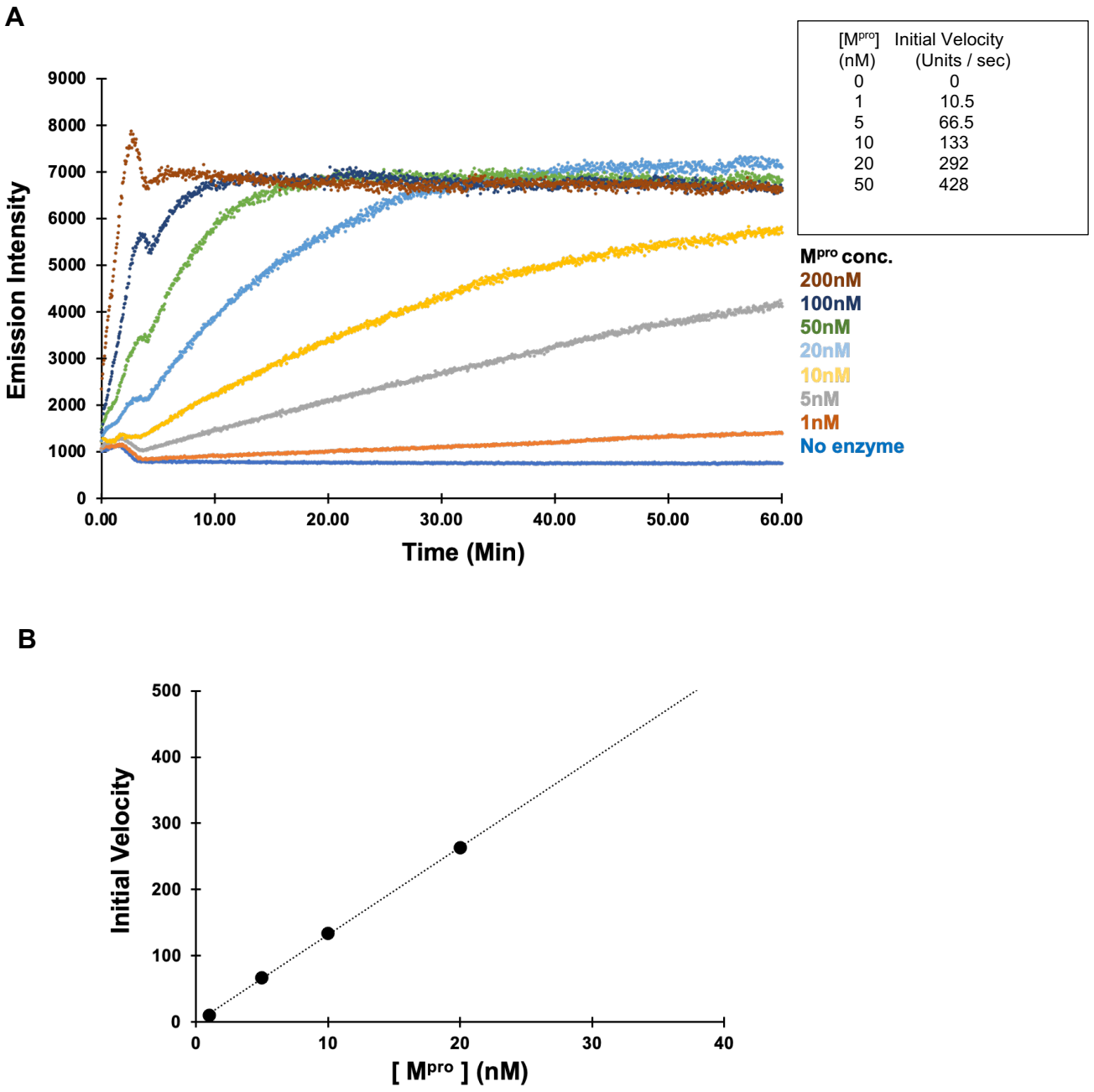

Fig. S2. Features of M^{pro} FRET proteolysis assay. Related to Figure 1E, and STAR Methods. (A) M^{pro} protease activity vs enzyme concentration using substate Dabsyl-KTSAVLQ/SGFRKME-Edans at pH 6.5 and 25 ºC, over the range of 0 to 200 nM M^{pro} concentration. Initial rates of hydrolysis measured at 0 to 50 nM enzyme concentration are indicted in the inset; at higher concentrations the rates were too fast to measure. For time points < 3 min, equilibration artifacts prevent reliable measurements. (B) Rates of hydrolysis (units / sec) are linear over the range 0 to 20 nM M^{pro} concentration.

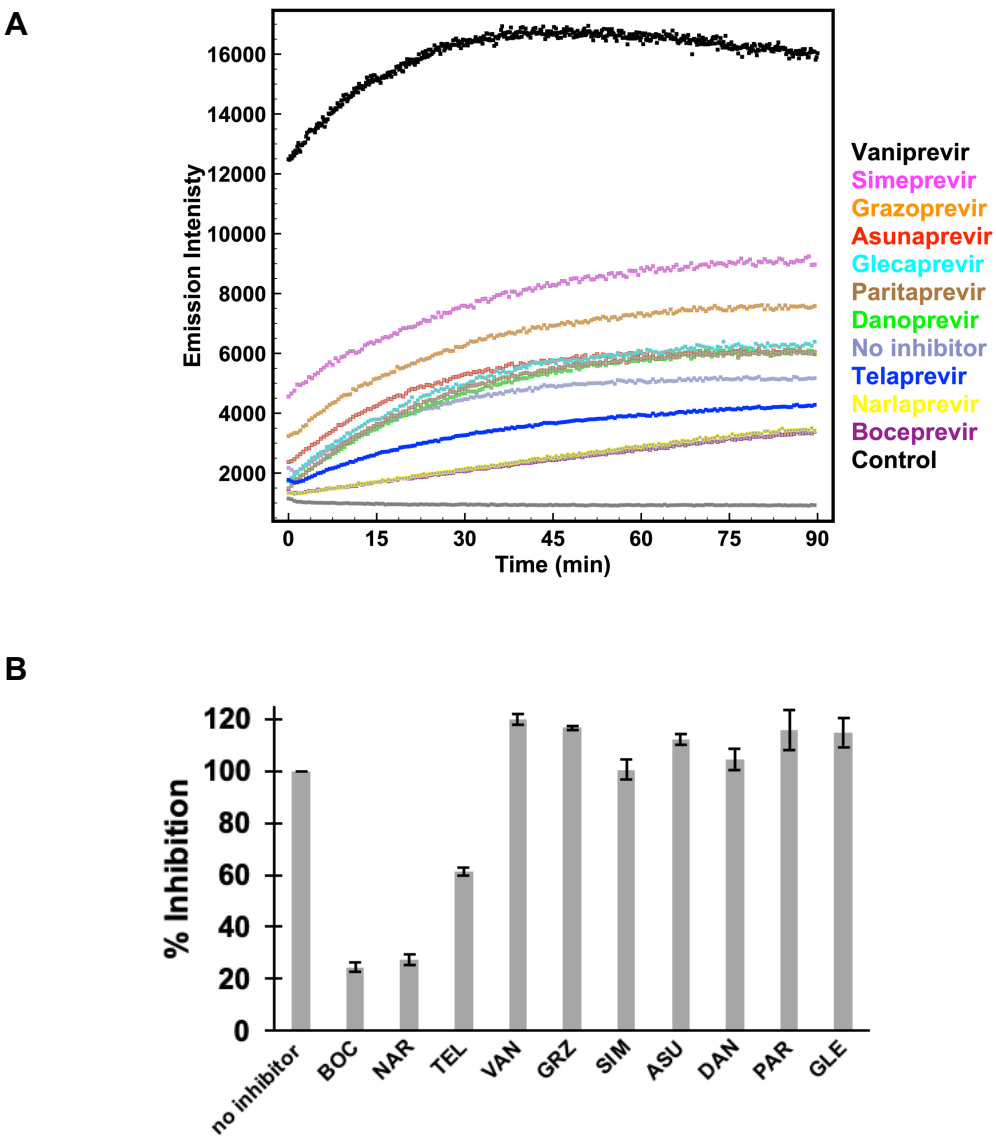

Fig. S3. SARS-CoV2 M^{pro} inhibition by HCV protease inhibitors. Related to Figure 1E, and STAR Methods. (A) Progression kinetics for M^{pro} were monitored in a FRET assay using substate Dabsyl-KTSAVLQ/SGFRKME-Edans at pH 6.5 and 25 ºC, under conditions outlined in the Star Methods. (B) Initial rates of proteolysis of a peptide substrate by M^{pro} in the presence of 20 μM inhibitor concentrations (v_i) relative to initial rate in the absence of inhibitor ($v_{i,o}$). Data for vaniprevir (VAN) has been corrected for inner filter effects, as outlined in STAR Methods and Supplementary Table S3.

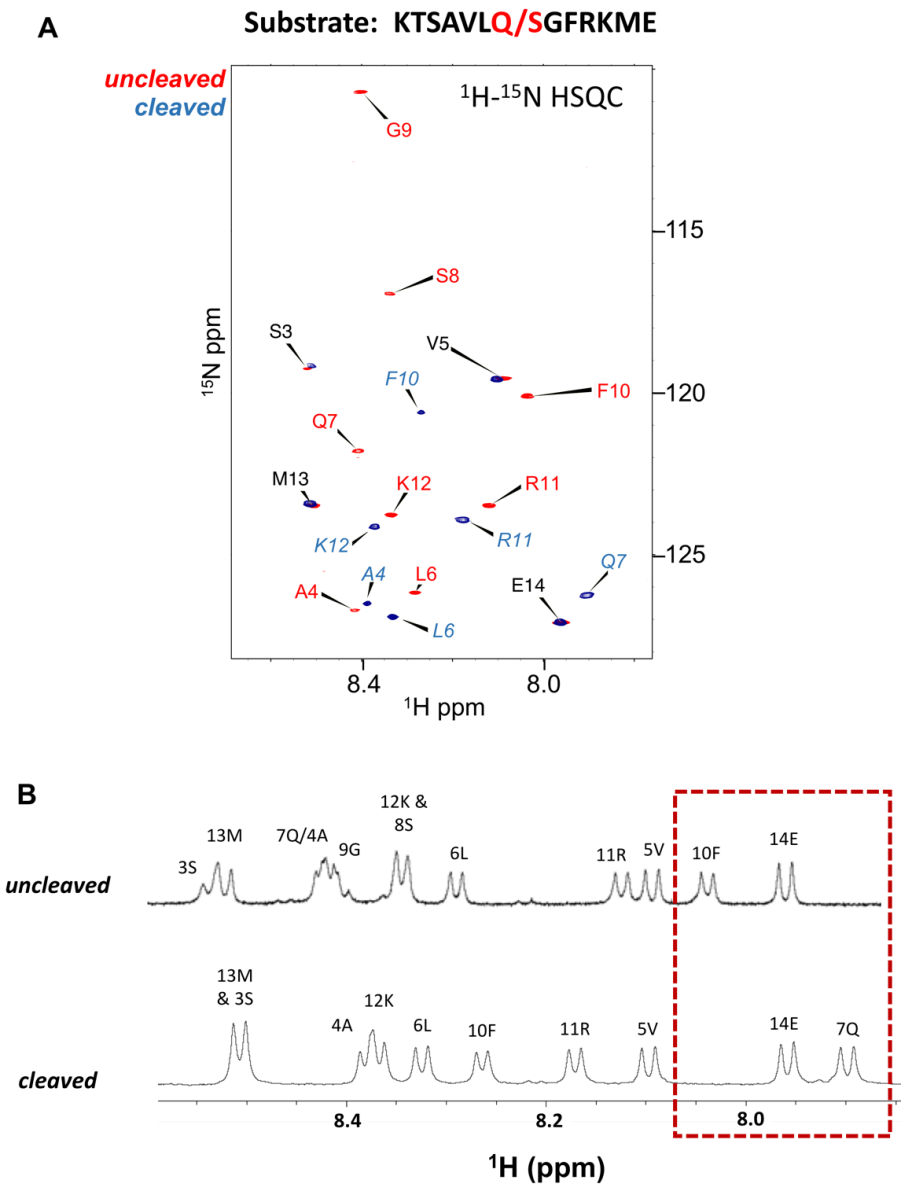

Fig. S4. Chemical shift assignments of backbone amide protons in uncleaved and cleaved M^{pro} peptide substrate. Related to Figures 1F-G, and STAR Methods. (A) Overlay of 2D ^{1}H-^{15}N HSQC spectra for uncleaved (red) and cleaved (blue) peptides (B) 1D ^{1}H spectra for cleaved and uncleaved peptides. Both spectra show changes in chemical shifts for some amino acids indicating proteolytic cleavage. These chemical shifts were determined at 25 °C using 2D COSY, TOCSY, and ^{1}H-^{15}N HSQC, along with 1D ^{1}H NMR experiments.

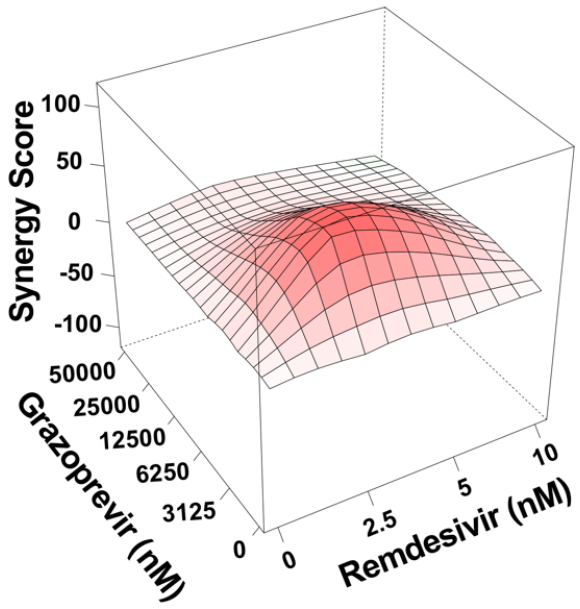

Fig. S5. Grazoprevir is also synergistic with remdesivir in an antiviral combination assay in human 293T cells. Related to Fig. 4. Human 293T cells were infected with SARS-CoV-2 in presences of two compounds titrated against each other in 2-fold serial dilutions and viral replication was determined using the immunofluorescence-based assay. As in Vero E6 cells (synergy score + 25.0), grazoprevir has positive ZIP synergy score (Ianevski et al., 2020) of + 20.3, indicative of its synergy with remdesivir.

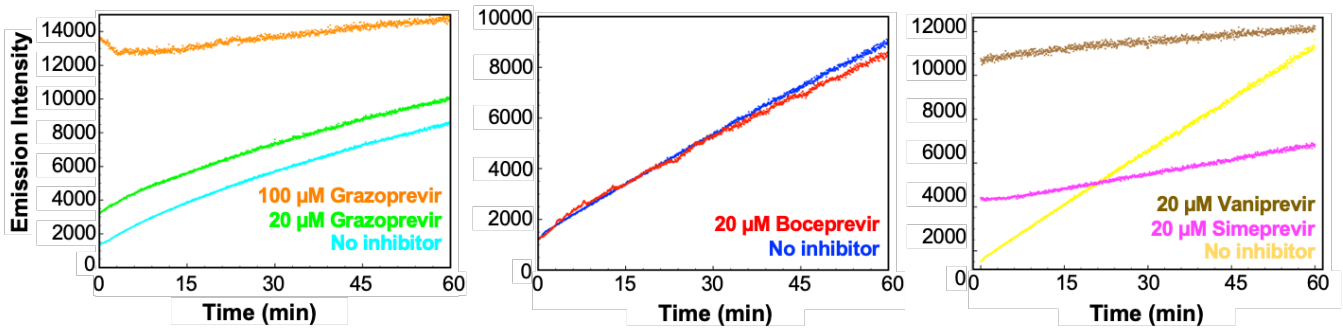

Fig S6. SARS-CoV-2 PL^{pro} inhibition by HCV protease inhibitors. Related to Figure 5B, and STAR Methods. Progression kinetics for PL^{pro} were monitored in a florescence assay using the fluorogenic substrate zRLRGG/AMC, at pH 7.5 and 25 ^{o}C, as outline in STAR Methods. 20 nM of PL^{pro} was incubated with 20 µM of HCV drugs. 20 µM substrate was added and the reaction was monitored for 2 hrs using the Infinite M1000 TECAN plate reader with filters for excitation at 360 nm and emission at 460 nm. These data document PL^{pro} inhibition by simeprevir and vaniprevir at 20 µM drug concentration, and grazoprevir at 100 µM drug concentration, with initial slopes less than that obtained in the absence of inhibitor. Boceprevir at 20 µM concentration does not inhibit PL^{pro}. The offsets at t=0 of emission intensity are due to the intrinsic fluorescence of the drugs.

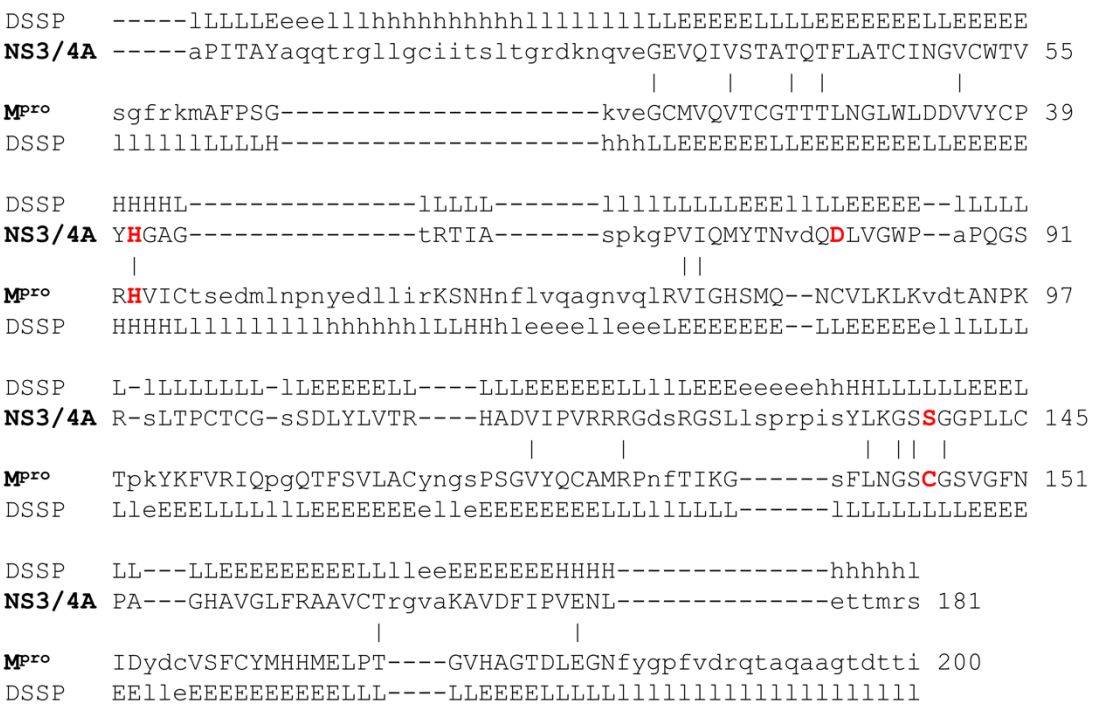

Fig. S7. Structure-based sequence alignment of HCV NS3/4A (NS3/4A) and SARS-CoV-2 M^{pro} (M^{pro}). Related to Figure 1A. The structure-based alignment results in alignment of key catalytic residues His41 and Cys145 of the SARS-CoV-2 M^{pro} with His57 and Ser139 of HCV NS3/4A protease, and some other substrate binding cleft residues. Catalytic residues of HCV NS3/4A (His57, Asp81 and Ser139) and SARS-CoV-2 M^{pro} (His41 and Cys145) are highlighted in bold red. Three-state secondary structure definitions by DSSP (H=helix, E=sheet, L=coil) are shown for each amino acid sequence. Structurally equivalent residues are in uppercase, structurally non-equivalent residues (e.g. in loops) are in lowercase. Identical amino acid are marked by vertical bars. This structure-based sequence alignment was generated using DALI (Holm and Sander, 1993, 1999).